Scale effects on marine cavitating flows: A study on a hydrofoil and a propeller operating in-behind condition

Citation for the original published paper (version of record):
Khraisat, Q., Persson, M., Everyd Bensow, R. (2026). Scale effects on marine cavitating flows: A study on a hydrofoil and a propeller operating
in-behind condition. Ocean Engineering, 351(Part 1).
http://dx.doi.org/10.1016/j.oceaneng.2026.124310

Ocean Engineering 351 (2026) 124310

Contents lists available at ScienceDirect

Ocean Engineering

journal homepage: www.elsevier.com/locate/oceaneng

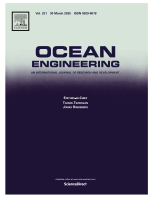

Research paper

Scale effects on marine cavitating flows: A study on a hydrofoil and a propeller operating in-behind condition

Qais Shehadeh Khraisat [a,*], Martin Persson [b], Rickard E. Bensow [a]

[a] Department of Mechanics and Maritime Sciences, Chalmers University of Technology, Chalmersplatsen 4, Gothenburg, 412 96, Sweden
[b] Kongsberg Hydrodynamic Research Center, Kristinehamn, 68193, Sweden

ARTICLE INFO

Keywords:
Cavitating hydrofoil
Cavitating propeller
Scale effects
Blockage effects
Pressure pulse levels

ABSTRACT

This paper investigates how scale effects affect the cavitating flow for two test cases of marine interest, using numerical simulations. The first is the Delft Twist 11 hydrofoil. Results show a larger cavity extent at full scale with earlier shedding; this behavior is related to changes in the pressure recovery on the foil at the closure region and a re-entrant jet that appears thicker and with higher momentum. Further modal analysis shows that scale effects are more pronounced in smaller-scale vapor structures while the large scale shedding dynamics is similar in both scales.

The second case investigates a cavitating propeller operating in a ship wake, assessing both scale effects and cavitation test blockage using small and large domains. The wakefield is strongly influenced by scale and blockage effects, which modifies the transient propeller loading. Less sheet and tip vortex cavitation are predicted at full scale or with a larger domain at model scale. This leads to lower predicted pressure fluctuations and pulse levels. Finally, assessment of using wall function approach for full scale simulations shows it underpredicts sheet and tip vortex cavitation.

1. Introduction

For a marine propeller to operate efficiently, it is optimized to generate high thrust while minimizing power input. Thus, propellers typically operate in a cavitating regime to minimize blade area and maximize the pressure difference between the suction and pressure sides. Cavitation refers to the formation of vapor pockets which can take many forms such as sheet, bubble, or tip vortex cavitation. It has several negative effects, causing induced vibrations from pressure fluctuations, material erosion, and underwater radiated noise that impacts marine life (van Terwisga et al., 2021). As a result, it is considered an important constraint during the design phase and is commonly investigated through model scale numerical predictions or experimental tests.

However, one of the main limitations of model testing in cavitation tunnels is the issue of scaling where it is not possible to achieve similarity with full scale condition (Billet and Holl, 1981). In cavitation tunnels where the free surface is not present, non-dimensional parameters including the Reynolds and cavitation numbers are considered for achieving flow similarity with the full scale condition. The cavitation number (σ) is used to match pressure conditions and achieve cavitation dynamics similarity. The Reynolds number (Re) accounts for viscous effects including boundary layer development and skin friction. However, achieving Re similarity in model tests is often impractical due to limitations in scale and velocity, which lead to discrepancies relative to ship scale (Billet and Holl, 1981; Larsson and Raven, 2010; Szantyr, 2006). The mismatch leads to variations in viscous forces and boundary layer development characteristics (Amromin, 2000). Furthermore, in addition to direct viscous scale effects on cavitation, the wakefield distribution upstream of the propeller will be affected. Differences in Re will influence both boundary layer development and the wakefield's spatial characteristics (Farkas et al., 2019). This is important as the spatial and temporal distribution of the wakefield play a significant role in the unsteady loading on the propeller and subsequently on cavitation (Regener et al., 2018).

The operation of propellers at a low Reynolds number in model scales promotes the formation of a laminar boundary layer over the blade surfaces. However, cavitation typically incepts in regions of instability such as the transition region in the boundary layer (Franc and Michel, 1985; Wang et al., 2001; Amromin, 2021). When laminar flow develops on the blade, it tends to delay and suppress cavity inception (Kuiper, 1978; Arakeri and Acosta, 1981; Ge et al., 2021). As a result, cavitation in model tests often appears unstable and intermittent (Dutweiler and Brennen, 2002). In contrast, at full scale, the flow over the blade is predominantly turbulent, and the laminar flow influence

* Corresponding author.
E-mail addresses: khraisat@chalmers.se (Q.S. Khraisat), martin.persson@km.kongsberg.com (M. Persson), rickard.bensow@chalmers.se (R.E. Bensow).

https://doi.org/10.1016/j.oceaneng.2026.124310
Received 1 November 2025; Received in revised form 22 December 2025; Accepted 13 January 2026
Available online 20 January 2026

becomes negligible. While the transition phenomena depend on the Reynolds number, the interaction of inertial and viscous forces is also significantly influenced by freestream turbulence. This is relevant to both scale effects and reliability of model tests as variations in freestream turbulence levels between testing facilities affect the cavitation inception (Korkut and Atlar, 2002).

Beyond viscous effects, water quality is also of importance in the context of cavitation. This refers to the distribution of nuclei and dissolved gas content within the liquid medium, where concentration and distribution of nuclei affect the formation and growth of cavitation bubbles (Holl, 1970). The presence of nuclei or dissolved gas has been found to reduce water tensile strength leading to cavitation inception at higher pressures compared to pure water (Apfel, 1970). In seawater, Gowing and Shen (2001) observed that nuclei size and number decrease with depth while oxygen content remains relatively stable. Therefore, achieving nuclei content similarity remains a challenge due to practical limitations and missing data on seawater in other areas.

Numerous model scale studies showed that nuclei content influences various cavitation types. Gindroz and Billet (1998) found that inception patterns of tip vortex cavitation are particularly sensitive to changes in nuclei concentration. The nucleus size is also shown to affect the vortex trajectory (Zhang et al., 2016). In hydrofoil experiments, the sheet cavity topology and shedding mechanisms have also been shown to be sensitive to nuclei content. Lower concentrations are shown to result in higher frequency shedding modes (Venning et al., 2017, 2018). Hilo et al. (2024) reported that air injection near the leading edge of a cavitating hydrofoil can reduce vapor content and noise, particularly in high frequency regions. They also report that as the cavitation number is reduced, noise reduction from air injection becomes less effective but shifts to lower frequencies. Similar findings are presented by Kamiirisa (2001), who reported that higher air content increases noise levels from cavitating propellers at lower frequencies but reduces them above 10 kHz. Such complexities of achieving nuclei content and distribution indicate that replicating seawater cavitation in test facilities requires precise control during tests. In addition to scale effects consideration, the reliability of model scale tests also suffers from variations in water quality (Tani et al., 2017). In a later study, Tani et al. (2020) reported results and measurements from seven different facilities, and large discrepancies were found in the cavitation due to many factors, including water quality.

The influence of object size on static pressure distribution is also of importance to scale effects for propellers. The similarity in the cavitation number between model and full scale can only be achieved at one given location, which is recommended to be close to the blade tip (ITTC 7.5-04-04-01, 2024). However, the static pressure distribution along the blade span will vary for different geometrical scales. The hydrostatic pressure contribution at full scale will be greater due to the larger depth which leads to different cavitation numbers along the blade span and affects cavitation inception (Szantyr, 2006). In addition, geometrically larger objects generate broader low pressure zones increasing the likelihood of nuclei initiating cavitation making full scale propellers more prone to cavitation inception than smaller models under similar conditions (Keller, 2001). Variations in time and velocity scales have also been shown to influence cavitation inception. Higher flow speeds promote cavitation due to stronger dynamic pressure fluctuations, lowering the threshold for nuclei destabilization (Keller, 2001).

Apart from experimental challenges associated with scale effects, efforts at numerical predictions for full scale cavitating propellers remain scarce within the research community. One of the earliest numerical studies on cavitation at full scale is presented by Ji et al. (2010) where the viscous RANS framework is used for a propeller in a non-uniform inflow condition. Comparisons with experimental pressure pulse measurements and cavitation observations showed good agreement for first-order levels which is associated with the good prediction of the sheet cavitation. However, the numerical models fail to predict the tip vortex cavitation due to limitations with numerical resolution, as well as the turbulence and mass transfer models. Similar underprediction of tip vortex cavitation is found even when using the higher fidelity Detached Eddy Simulation (DES) (Ponkratov, 2015). Li et al. (2018) investigated the full scale ship under cavitating conditions with a focus on hydroacoustic assessment using DES in combination with the FW-H acoustic analogy. While sheet cavitation was well predicted and reasonably agreed with full scale observations, the strength and extension of the tip vortex were underpredicted leading to discrepancies in the noise signature.

Yang et al. (2013) investigated scale effects on cavitation using three geometrically similar propellers of different scales operating under non-uniform inflow conditions. They found that both the cavitation inception number and cavity area ratio increased with larger geometrical scales. In addition, the predicted noise spectrum levels increased and the dominant tonal noise frequencies shifted under identical conditions. However, the chosen time-step corresponding to 2 degrees of blade rotation may lack resolution to resolve cavitation dynamics. Soydan and Bal (2021) reported similar findings on the cavitation extent for a propeller operating in a uniform flow. Sakamoto and Kamiirisa (2018) investigated a cavitating propeller at model and full scales using DES, and later Brown's semi-empirical approach for estimation of the broadband noise upper bound. Their study showed that scale effects on cavitation strongly affect noise predictions as higher Reynolds number increases cavitation extent, dynamics, and resulting noise compared to model scale. Viitanen et al. (2020) performed numerical simulations for a propeller in open water conditions. While a grid sensitivity study is performed, the resolution of grids may potentially underpredict the cavitation, its dynamics, and the small scale structures at full scale. This is indicated by the observed higher rate of dissipation for the tip vortex at the full scale condition. In this study, a larger extent of cavitation for higher Reynolds number is also reported. Sezen and Atlar (2022) carried out full scale CFD simulations for a propeller operating in-behind while primarily focusing on underwater radiated noise prediction and comparison against sea trial data. Again, the tip vortex and its dynamics were underpredicted but no comparisons with model scale condition are presented.

Despite the extensive research on cavitation, studies on scale effects on the cavitating flow through comparison between model and full scale conditions remain limited. In this paper, a numerical investigation is performed with a focus on the influence of scaling between typical ship cavitation tests and the full scale ship on the characteristics of the resulting cavitating flow. The objective is not to resolve the fundamental scale effects on cavitation and associated physical mechanisms, but rather to perform a global analysis within the practical limitations of the chosen numerical methods and study the effects on propeller cavitation simulations. Two test cases and geometries are considered where each features different types of cavity structures.

The first geometry is the Delft Twist 11 hydrofoil where cavitation is characterized by unsteady shedding behavior (Foeth, 2008). This flow is well studied in model scale, and while large scale data are not available we use it here to represents an idealised flow that is familiar to the community. Here, the analysis focuses on the influence of scale on pressure distribution, developed vapor structures, shedding behavior, and modal decomposition of the cavitation dynamics using the Proper Orthogonal Decomposition (POD) technique. Results are compared with model scale tests done at Delft University of Technology (TU Delft) and École Polytechnique Fédérale de Lausanne (EPFL) cavitation tunnels.

The second case is a propeller operating within the wakefield the ship hull where sheet and tip vortex cavitation develop. The analysis is focused on scale together with blockage effects on cavitation. Results on wakefield, pressure distribution on propeller blades, cavitation dynamics, pressure fluctuations, and pressure pulse levels are presented. Finally, a brief evaluation on computational efficiency at full scale is provided by comparing results from wall-resolved and wall-function approaches.

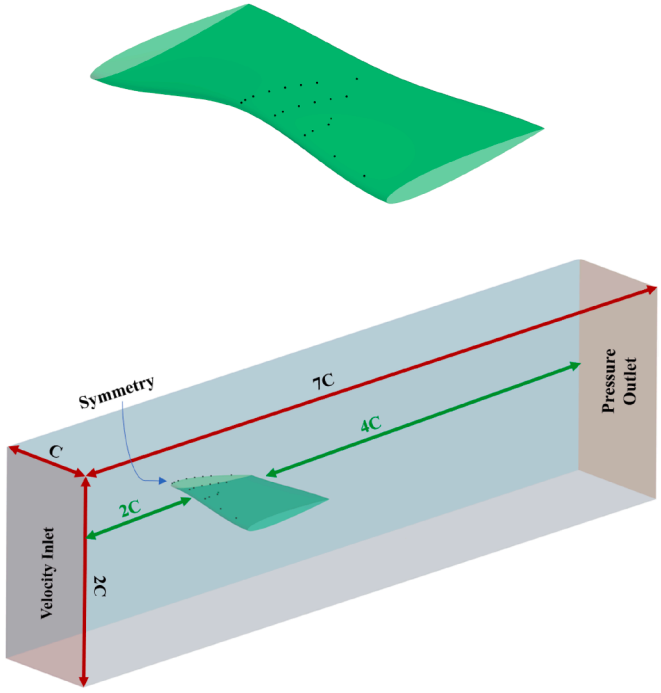

Fig. 1. Delft Twist 11 hydrofoil geometry (top) and computational domain with boundary conditions (bottom).

2. Case description

2.1. Delft twist 11 hydrofoil test case

The Delft Twist 11 hydrofoil geometry was extensively investigated by Foeth (2008) and first studied numerically by Huuva (2008). It was later also introduced at the Second International Symposium on Marine Propulsors (smp'11). The geometrical profile of the foil is a NACA0009 with a chord length of 150 mm and a span of 300 mm. A key feature of the foil design is the symmetric spanwise variation in the angle of attack (AOA) which ranges from 0^o at the foil side edges to 11^o at the centerline. This gradual change in the angle of attack induces load variations across the upper side resulting in a three-dimensional cavity. Further details on the geometry are presented in Foeth and van Terwisga (2006). Experimental studies were conducted in the cavitation tunnels at TU Delft and on a geometrically smaller model at École Polytechnique Fédérale de Lausanne (EPFL). To mitigate the influence of a developing laminar boundary layer on cavity inception, rough elements were applied to the leading edge of the foil. These elements have an estimated height of 120 μm and cover up to 4 % of the chord length. Both wetted and cavitating flow experiments were performed across a range of different angle of attacks. In this paper, the numerical simulations focus on the specific case where the foil is set at an AOA of -2^o.

The computational domain dimensions follow the guidelines provided for the workshop at smp'11, which in turn were based on the dimensions of the cavitation tunnel at TU Delft. As shown in Fig. 1, the foil is positioned two chord lengths from the inlet boundary to the leading edge and four chord lengths from the trailing edge to the outlet boundary. Slip wall boundary conditions are applied to the top, side, and bottom walls. Fixed velocity and pressure conditions are specified at the inlet and outlet boundaries. To reduce computational cost, only half of the foil is modeled with a symmetry boundary condition at the centerline plane. No-slip wall boundary conditions are imposed on the foil surfaces. To investigate scale effects on cavitation, a geometrically scaled-up model with a scale ratio of $\lambda = 20$ is used. The computational domain dimensions are scaled by the same ratio.

Table 1
Tanker characteristics at full scale.

	Ship Data
Length between perpendiculars, Lpp	144.3 m
Ship draught, T	8.7 m
Number of propellers	1
Number of blades, Z	4
Direction of rotation	Left hand
Propeller diameter, D	5.7 m
Blade area ratio, A_E/A_O	0.376
Design pitch ratio, P/D	0.978
Blade tip clearance	0.28 × D
Chord length 0.75R	1.25 m

At the small scale, the numerical boundary and operating conditions are aligned with the experiments. A fixed inlet flow velocity of 6.97 m/s is applied with water density and dynamic viscosity set to 998 kg/m^3 and 9.27×10^{-4} Pa·s, respectively. With these conditions, the smaller scale operates at a Reynolds Number of 1.1×10^6. At the large scale, the Reynolds number increases to 2.58×10^7. For both scales, the reference pressure is adjusted to maintain a cavitation number of $\sigma = 1.07$, similar to the experiments. With these conditions, non-dimensional lift coefficient similarity is achieved between the two scales with a relative difference of 1.1 %. Throughout the paper, the smaller and larger scale conditions for the foil case are referred to as the model scale and full scale, respectively.

2.2. Propeller behind ship hull test case

A moderately skewed, controllable-pitch, four-bladed propeller is mounted behind the hull of a chemical tanker as shown in Fig. 2 (Left). The main characteristics of the ship, including the propeller, are summarized in Table 1.

Model scale pressure pulse measurements were conducted by RISE in their cavitation tunnel following ITTC recommended procedures and guidelines for model scale cavitation tests. Tunnel Section 3 was used and has dimensions of 8.0 m in length, 2.10 m in width, and 1.22 m in height. The hull draft is increased compared to the fully loaded design condition at ship scale. Tunnel pressure is adjusted to achieve the desired cavitation number based on pressure measurements at the propeller shaft centerline. To ensure non-dimensional similarity of thrust and torque coefficients, the propeller rotation rate is modified during the tests. Due to operational constraints at the experiments, it was not possible to replicate the full scale Continuous Service Rating (CSR) condition. As a result, two sets of model scale numerical simulation are performed that match both the experimental and CSR conditions.

Cavitation patterns and behavior are captured using camera recordings with a frame rate synchronized to the shaft rotational frequency. Induced pressure pulse fluctuations are measured with eight piezoelectric pressure sensors, and their configuration is presented from a top-view perspective in Fig. 2.

Fig. 2. Ship mounting in RISE cavitation tunnel (left) and top view for the pressure transducers placement during the model tests.

Table 2
Non-dimensional similarity for cavitating propeller at model and full scale conditions.

	RISE Experiment	CFD RISE Cond.	CFD TS (CSR)	CFD LD (CSR)	CFD FS (CSR)
N (rps)	24	24	20	20	20
K_T	0.171	0.174	0.188	0.187	0.181
K_Q	0.0265	0.0273	0.0289	0.0289	0.0298
$\sigma_{0.7R}$	7.84	7.84	6.86	6.86	6.86
Re (propeller)	$5.0{\cdot}10^5$	$5.0{\cdot}10^5$	$4.2{\cdot}10^5$	$4.2{\cdot}10^5$	$2.3{\cdot}10^7$

Numerical simulations at model scale are performed based on the operating conditions during the experiments as well as the continuous service rating at full scale. The geometrical scaling ratio λ is 27.14. At model scale, the computational domain dimensions are set to match the RISE cavitation tunnel, whereas the full scale domain is extended based on the ship length between perpendiculars to simulate free-field conditions and mitigate the influence of boundaries on the solution. As shown in Fig. 3 (bottom), the inlet is extended $2L_{pp}$ from the bow, $3L_{pp}$ from the stern, and the domain total depth and width are also set to $3L_{pp}$. While the hull draft is increased at the model scale experiments, the design draft is simulated at the full scale condition. Based on the operating conditions summarized in Table 2, the propeller Reynolds number at model and full scale conditions are $5.0 \cdot 10^5$ and $2.3 \cdot 10^7$, while it is $2.1 \cdot 10^7$ and $9.3 \cdot 10^8$ for the hull.

To evaluate blockage effects caused by the confined space of the tunnel section, an additional model scale simulation at the CSR condition is performed using a larger domain that extends the inlet, outlet, side, and bottom boundaries. In this work, the tunnel section and large domain are abbreviated as TS and LD, respectively. Due to the increase of the domain size in the LD condition, the inlet velocity is adjusted while maintaining a fixed rotation rate to ensure similarity in propeller loading. A summary of the operational conditions is provided in Table2. In the numerical simulations, to achieve non-dimensional similarity and match the propeller loading conditions relative to the full scale condition and model tests, the thrust coefficient K_T, torque coefficient K_Q, and cavitation number σ are defined as follows,

$$K_T = \frac{T}{\rho n^2 D^4}, \tag{1a}$$

$$K_Q = \frac{Q}{\rho n^2 D^5}, \tag{1b}$$

$$\sigma = \frac{P_s - P_v + P_h}{0.5\rho V_A^2}, \tag{1c}$$

where T is propeller thrust, ρ is water density, n is propeller rotation rate, D is propeller diameter, Q is propeller torque, P_s is static pressure, P_v is vapor pressure, P_h is hydrostatic pressure, and V_A is advance velocity, calculated based on the propeller advance coefficient J.

3. Numerical approach

All simulations are carried out using the commercial software package Simcenter STAR-CCM+. The built-in meshing tools are used for domain discretization. The Trimmer Mesher is applied to discretize the computational domains in all cases, except for the rotating propeller region, where the Polyhedral and Advancing Layer Mesher (ALM) is used. A mean y^+ value below 1.0 is maintained to resolve the boundary layer on the hydrofoil, propeller, and hub. However, the wall function approach is adopted for the hull and rudder at full scale condition. The wall boundary is modeled using the all-y^+ approach, which employs blending functions for turbulent kinetic energy production and dissipation.

In the hydrofoil case, the grid resolution is refined on the upper side and extended downstream within the core mesh, as shown in Fig. 4 (top), to capture the dynamics of the transported cloud cavity. Similarly, in the propeller in-behind case, a curved cylindrical control volume is used to resolve the tip vortex cavitation with high spatial resolution. A summary of the generated grids for both the hydrofoil and propeller cases is provided in Tables 3 and 4, respectively.

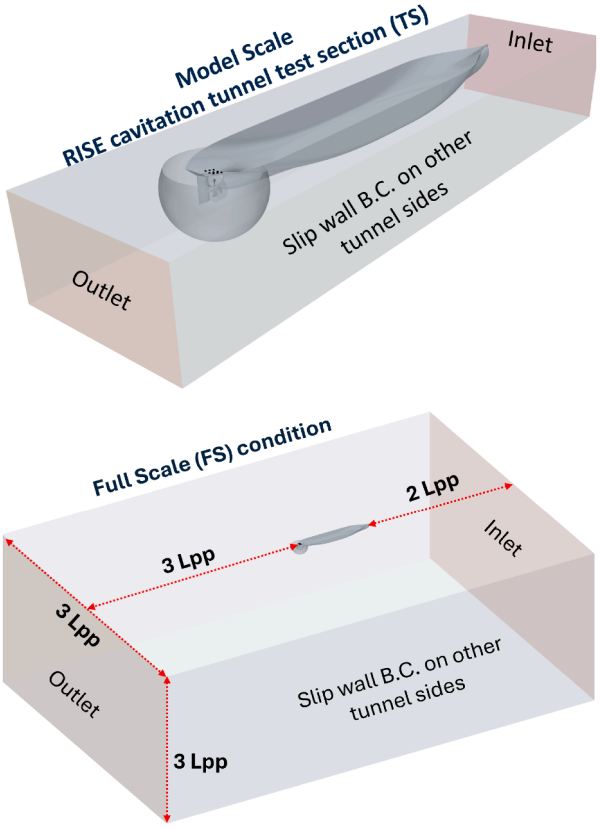

Fig. 3. Computational domains for model scale tunnel section (TS) that is sized to match the RISE cavitation tunnel (top), and full scale domain designed to mimic open waters condition (bottom).

Cavitation is modeled using a single fluid approach, where the liquid and vapor phases are treated as a homogeneous mixture. The fluid is assumed to be incompressible with the mixture density varying based on the local volume fraction α_v, represented by a ratio of the vapor and liquid content. The continuity and momentum equations are solved for the mixture as a whole, rather than for the individual phases. The mixture density and dynamic viscosity are defined as,

$$\rho_m = \alpha_v \rho_v + (1 - \alpha_v)\rho_l, \tag{2}$$

$$\mu_m = \alpha_v \mu_v + (1 - \alpha_v)\mu_l, \tag{3}$$

where μ is the dynamic viscosity. Subscripts m, v, and l correspond to the mixture, vapor, and liquid phases, respectively.

An additional transport equation is needed to solve for the local volume fraction α_v,

$$\frac{\partial \alpha_v}{\partial t} + \nabla(\alpha_v u) = \frac{\dot{m}}{\rho}, \tag{4}$$

where $\dot{m}$ represents the mass transfer rate source term for vaporization and condensation. The Schnerr-Sauer mass transfer model is used (Schnerr and Sauer, 2001), and the local volume fraction α_v is defined as the

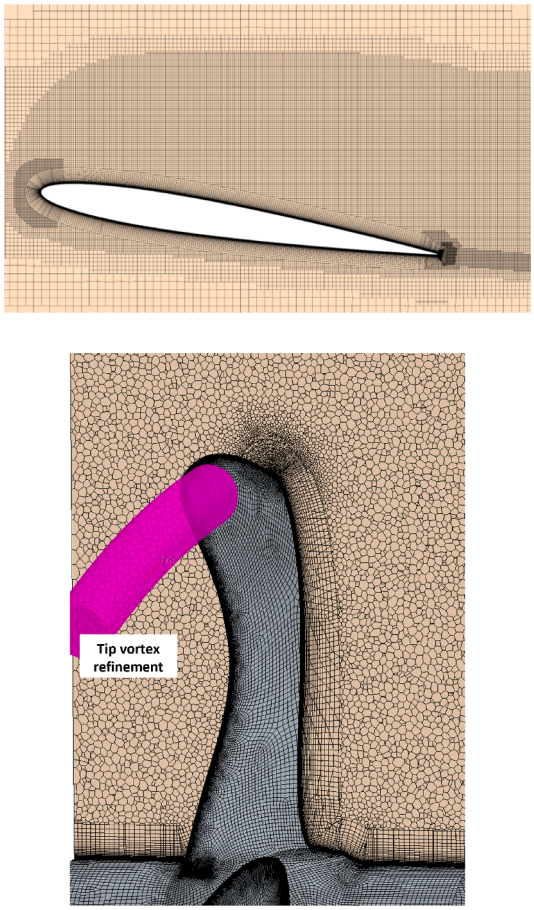

Fig. 4. Cross-section views of the grids for Delft Twist 11 hydrofoil (top) and Propeller (bottom) cases.

Table 3
Delft Twist 11 grid details for model and full scale conditions.

	Small Scale	Large Scale
Mean y^+	0.25	0.35
Number of prism layers	48	66
Growth ratio	1.14	1.14
Cell count (million)	16.55	37.2

Table 4
Grid details for the ship at model and full-scale conditions.

	Model Scale	Full Scale
Hull mean y^+	0.55	75
Propeller mean y^+	0.28	0.08
Number of prism layers (propeller)	47	83
Growth ratio	1.15	1.15
Cell count (million)	59.8	63.5

ratio between the local vapor volume and the cell volume,

$$\alpha_v = \frac{V_v}{V_{cell}} = \frac{n_0 \frac{4}{3}\pi R^3}{1 + n_0 \frac{4}{3}\pi R^3}. \tag{5}$$

Here, n_0 represents the initial number of bubbles per unit volume of liquid, and R is the bubble radius. All bubbles are initially assumed to be of equal size. The rate of change of the volume fraction is given by,

$$\frac{d\alpha_v}{dt} = \alpha_v(1-\alpha_v)\frac{3}{R}\frac{dR}{dt}. \tag{6}$$

Effects of bubble acceleration, viscous forces, surface tension, and velocity slip between vapor bubbles and the liquid are neglected. The resulting rate of change for bubble growth and collapse is reduced to,

$$\frac{dR}{dt} = -\text{sign}(P(R) - P_\infty)\sqrt{\frac{2}{3}\frac{|P(R) - P_\infty|}{\rho_l}}, \tag{7}$$

where $P(R)$ represents the internal pressure of the bubble and P_∞ is the far-field pressure. The mass transfer source term for vaporization and condensation is defined as,

$$\dot{m} = \begin{cases} C_c \frac{\rho_l \rho_v}{\rho_m}\frac{d\alpha_v}{dt}, & \text{if } P(R) > P_v \\ C_v \frac{\rho_l \rho_v}{\rho_m}\frac{d\alpha_v}{dt}, & \text{if } P(R) \le P_v \end{cases} \tag{8}$$

The condensation C_c and vaporization C_v constant terms are both set to 1.0 which is the default setting. The initial number of bubbles per unit volume of liquid n_0 and diameter are set 10^{12} m^{-3} and 10^{-6} m, respectively.

The Reynolds-Averaged Navier-Stokes (RANS) approach is used in the simulations. Mass and momentum equations for the mixture are defined as follows,

$$\frac{\partial(\rho_m)}{\partial t} + \nabla \cdot (\rho_m U_m) = 0, \tag{9}$$

$$\frac{\partial(\rho_m U_m)}{\partial t} + \nabla(\rho_m U_m U_m) = -\nabla p + \nabla(\tau - \rho_m \overline{u'u'}) + f. \tag{10}$$

Here, U_m is the average mixture velocity, p is the pressure, τ is the viscous stress tensor, f is body forces, and $-\rho_m \overline{u'u'}$ is the Reynolds stress tensor. In the case of the hydrofoil computations, the Boussinesq approximation is used for the Reynolds stresses which assumes a linear constitutive relation with the mean strain rate S,

$$-\rho_m \overline{u'u'} = 2\mu_T S - \frac{2}{3}\rho_m k I, \tag{11}$$

where k is the turbulent kinetic energy, and I is the identity matrix.

For the in-behind propeller case, the Boussinesq approximation is extended to account for turbulence anisotropy using a Quadratic Constitutive Relation (QCR) (Spalart, 2000; Software, 2023). This modification introduces non-linear terms based on the strain and vorticity rate tensors, and improves turbulence predictions in flows with strong secondary motions, high streamline curvature, or highly non-equilibrium conditions (Sabnis et al., 2021; Su and Yuan, 2017; Software, 2023). The additional computational cost from the extra gradient terms is negligible.

Eddy viscosity is modeled with the $k-\omega$ SST turbulence model (Menter et al., 2003) which uses the strain rate S to calculate the eddy viscosity μ_T,

$$\mu_T = \frac{\rho k}{\min(\frac{a^*}{\omega}, \frac{a_1}{SF_2})}, \tag{12}$$

where a_1 and a^* are model constants, k is the turbulent kinetic energy, ω is the specific dissipation rate, and F_2 is a blending function. The calculation of the eddy viscosity remains unchanged when using the QCR formulation.

Standard Reynolds-Averaged Navier-Stokes (RANS) models were originally developed for single-phase flows. One limitation when applying them to multiphase flows is their tendency to predict excessive eddy viscosity levels in mixture regions (Reboud et al., 1998). This issue is particularly relevant in cases of shedding cloud cavitation where the excessive eddy viscosity suppresses the formation of the re-entrant jet, a mechanism important for unsteady cavity dynamics. Without a correction, the solution converges to a steady and fully attached cavity (Coutier-Delgosha et al., 2003; Bensow, 2011), not representative for the dynamics of sheet cavitation.

To address this limitation, the empirically proposed Reboud correction (Reboud et al., 1998) is applied. It modifies the turbulent viscosity

in the mixture region and has been used in both hydrofoil and propeller cases. The correction function is defined as,

$$f(\rho) = \rho_v + \left(\frac{\rho_v - \rho}{\rho_v - \rho_l}\right)^n (\rho_l - \rho_v), \tag{13}$$

where n is a constant set to the recommended value of 10. The correction is only active in the mixture regions.

The flow is assumed to be incompressible, and the segregated solver is used to solve for the mass and momentum equations using the pressure-based SIMPLE algorithm for pressure-velocity coupling. Second-order convection schemes are applied for both velocity and turbulence quantities. A steady-state solution is first obtained and then used to initialize the transient computations.

For the hydrofoil case, the time step is set to 5×10^{-5} s for the model scale and 2×10^{-4} s for the full scale. This corresponds to approximately 616 time steps per shedding cycle for the model scale and 2642 for the full scale. A finer time resolution is required at full scale to maintain numerical stability and to resolve the cloud cavity dynamics. For the propeller in-behind, the time step size at both model and full scale is selected to match a propeller rotation increment of 0.25^o per time step. In both propeller and hydrofoil cases, 20 inner iterations per time step were used.

4. Results and discussion

4.1. Cavitating delft twist 11 hydrofoil

4.1.1. Pressure distribution on foil upper side

The predicted time-averaged pressure distribution is presented in Fig. 5 for spanwise locations at 40 % and 50 % of the total span together with experimental measurements. The y-axis represents the non-dimensional pressure coefficient (-Cp), defined the local static pressure normalized by hydrodynamic component $0.5\rho V^2$, where V is the velocity magnitude. The non-dimensional chord length (x/C) is shown on the x-axis with zero corresponding to the leading edge of the foil. In the numerical simulations, statistics of the pressure distribution were collected and averaged over 15 shedding cycles. While averaging over longer time intervals would improve statistical convergence, 15 shedding cycles are deemed sufficient for the analysis of the unsteady phenomena presented here. Reasonable agreement between numerical predictions and EPFL measurements is obtained with a slight overprediction in pressure levels from the numerical results at both span locations. However, larger differences are obtained when compared to the TU Delft measurements. These measurement points are however questionable as they present pressure levels that are significantly below the vapor pressure for the studied condition. The exact reason for the consistently overprediction of pressure levels in the numerical results is difficult to assess from available results. As this represents time-averaged pressure, the values are affected by the predicted cavity development and extent which has been shown to be influenced by the tripping used in the experiments (Asnaghi and Bensow, 2020) and inflow turbulence (Klapwijk et al., 2021), neither which is considered in this study. The differences between model and full scale at the closure of the cavity at the centreline can however plausibly be connected to different development of the re-entrant jet in the two conditions.

At 50 % span, it is interesting to note the gradual increase in the pressure level by the numerical predictions from the leading edge up to 0.15 x/C at both model and full scale conditions, which is not as pronounced in the experiments. This may be due to the sandgrain roughness along the leading edge in the experiments, but possibly also not detectable due to missing pressure probe data in that region. In addition, the increase in pressure levels in that region is not clear at 0.4 span, pointing to a possible connection with the re-entrant jet interfering with the formation of the sheet cavity. Another key observation related to scale effects is at the cavity closure region ($0.45 < x/C < 0.55$). Here, the pressure levels at full scale are different than at model scale which will influence

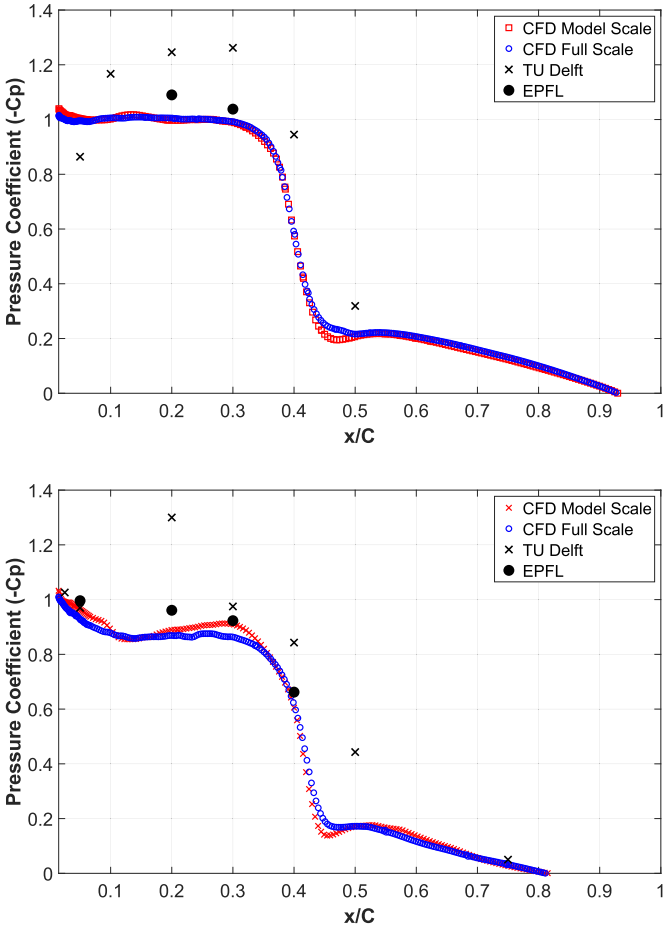

Fig. 5. Pressure distribution on the Delft Twist 11 upper side: 40 % span (top) and 50 % span (bottom).

the pressure-driven re-entrant jet. This appears to result in a re-entrant jet with higher momentum shifting the shedding frequency as shown in the subsequent section.

4.1.2. Cavitation pattern and shedding behavior on the hydrofoil

Analysis of the cavity pattern and shedding behavior is provided at different time instants for one typical shedding cycle in Fig. 6. The instantaneous snapshots are shown for the predicted cavity for both model (middle) and full scale (right) conditions together with experiments from TU Delft (left). The vapor structures are visualized with an isosurface for the volume fraction of vapor set at $\alpha_v = 0.5$. Vortical structures are shown with the normalized Q-criterion, $Q^* = \frac{Q}{U_\infty/c^2}$ where c and U_∞ are the chord and free-stream velocity. The limiting streamlines represent the vector direction of the wall shear stress.

The shedding of the attached cavity is due to the instability driven by the re-entrant jet. As the attached cavity develops, higher stagnation pressure develops at the closure of the sheet as the main flow curves toward foil surface. As a result, a small layer of liquid flows underneath the cavity and towards the leading edge. In the case of the Delft Twist 11, the re-entrant jet has two components, as described by Foeth and van Terwisga (2006). The first component travels upstream and perpendicular to the cavity closure and is called the re-entrant jet. The second folds around the sides of the sheet cavity and is called the side-entrant jet. While it also moves upstream toward the leading edge, the side-entrant jet is characterized with a spanwise velocity component. As both jet components near the foil leading edge, they cause the attached cavity to break off, forming a traveling vapor cloud in the downstream direction.

Good agreement is obtained between the numerical predictions and experiments for the global cavitation shedding behavior and mechanisms. The side-entrant jet can be seen in the first four snapshots in Fig. 6. In this region, the isosurface of Q^* shows that it is rich with small-scale vortical structures. These structures remove vapor from the attached sheet and entrain them in the downstream direction. The numerical predictions appear to underpredict the volume of entrained vapor. In addition to the previously mentioned differences in set-up related to tripping and free stream turbulence, the RANS framework may contribute. Comparing model and full scale conditions, the cavity extension is slightly larger at full scale. This is linked to lower pressure levels near the cavity closure region, which also affects the pressure-driven re-entrant jet as discussed below. In addition, a cloud structure appears downstream of the cavity closure. The numerical models predict a horse-shoe vortex structure in the cloud in both model and full scale conditions. While it is not clear in these experimental snapshots in this view, this structure has previously been noted in model scale experiments and now shown to appear also in full scale.

The fourth time instant shows a comparison for the detachment of the cavity. As mentioned earlier, the re-entrant jet causes the attached cavity to separate from the surface as it nears the leading edge. It is observed that the time instant of the detachment is different and occurs slightly earlier at the full scale condition. At that same time instant at model scale, the jet has not yet reached the leading edge, and the cavity remains attached. This is believed to be associated with two aspects. First, the observed pressure level and pressure gradient at the cavity closure at full scale , with a higher pressure downstream the cavity closure and lower pressure in the closure region, drives the re-entrant jet underneath the cavity with higher momentum leading to earlier detachment; the mechanisms for this development is detailed by e.g. Arabnejad et al. (2019). Second, the difference in Reynolds number and the ratio of inertial to viscous forces makes viscous effects more pronounced at model scale. As a result, the viscous losses on the jet at model scale are more significant. This is visualised by the instantaneous pressure distribution (-Cp) collected near the cavity closure as shown in Figs. 7 and 8. Data is collected using a line probe that is perpendicular to the foil surface and positioned at 0.3 of the chord. The pressure levels near the wall are lower at full scale and up to the vapor structure, reflecting that the re-entrant jet is driven with higher velocity.

After the main and side-entrant jet components reach the leading edge, the cavity detaches forming a traveling cloud as shown in the sixth time instant. The cloud is characterized by a spanwise vortex structure at both model and full scale conditions. A secondary vortex, with its axis of rotation in the wall-normal direction, starts to develop in the seventh snapshot. This wall-normal vortex then evolves into a horse-shoe structure that carries vapor within its core, which is visible in the last two snapshots. In the final snapshot, the spanwise vortex structure has diminished and appears similar at both scales. The irregular nature of the cloud makes averaged observations of scale effects difficult. Despite this, scale effects appear to not change the global behavior or shedding mechanism of the hydrofoil. However, smaller scale vortical structures are more pronounced at the full scale condition, which is due to the differences in Reynolds number and broader energy spectrum.

To identify the shedding frequency of the cloud, the Fast Fourier Transform FFT is applied to the collected vapor volume data over 15 shedding cycles. The predicted frequency at model scale shows good agreement with experimental measurements. In the TU Delft tests, the reported shedding frequency is 32.5 Hz, which closely matches the numerical predictions at 32.48 Hz. This corresponds to a Strouhal number of 0.699 at model scale, calculated based on foil chord. At full scale, the predicted shedding frequency is 1.89 Hz, resulting in a Strouhal number of 0.71. The change in the Strouhal number suggests a shift in the shedding frequency due to scale effects on the cavity extent and the dynamics of the re-entrant jet.

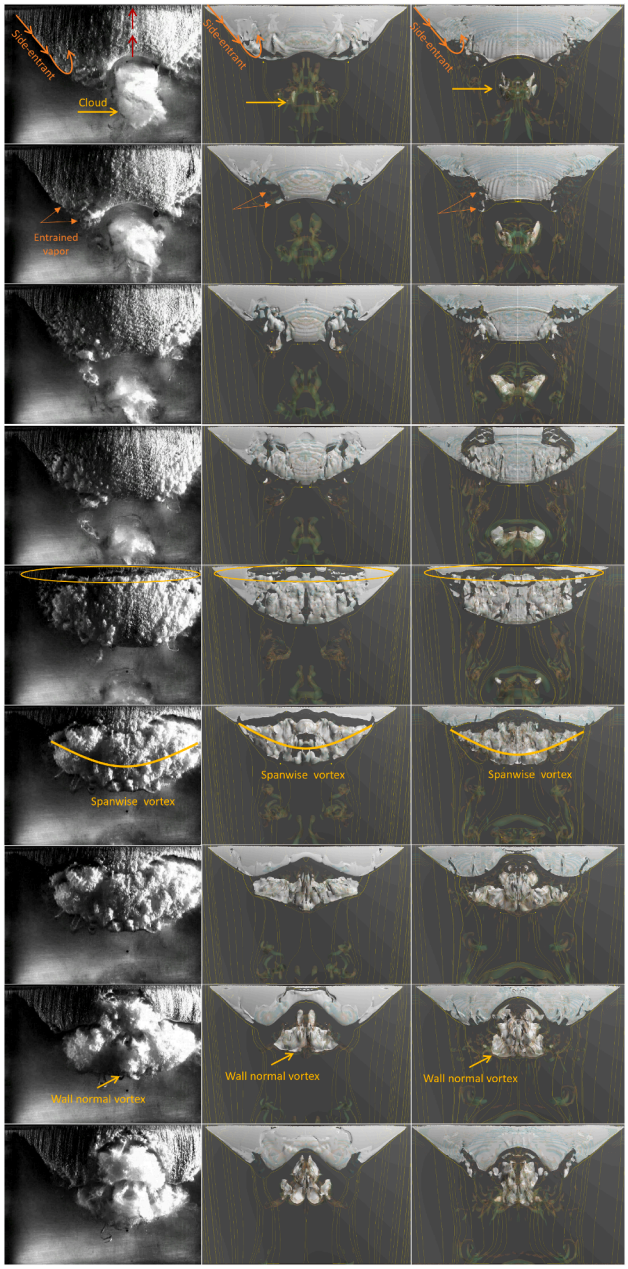

Fig. 6. Instantaneous snapshots for the time evolution of the shedding cloud. Left column shows experiments, middle shows model scale, and right shows full scale.

4.1.3. *Proper orthogonal decomposition: modal analysis on vapor structures*

To investigate further the scale effects on the vapor structures, Proper Orthogonal Decomposition (POD) (Moin, 1992) is applied to a series of two-dimensional snapshots of the transient cavitation. Here, the goal is to decompose the dataset into a set of orthogonal basis modes that represent the dominant spatial structures and their corresponding temporal evolution. The decomposition allows to identify coherent vapor structures and the key dynamics of the cloud shedding which correspond to the highest energy contributions. The separation of the spatial and temporal variables is achieved by,

$$Y(x,t) = \sum_{i=1}^{N} a_i(t)\phi_i(x), \tag{14}$$

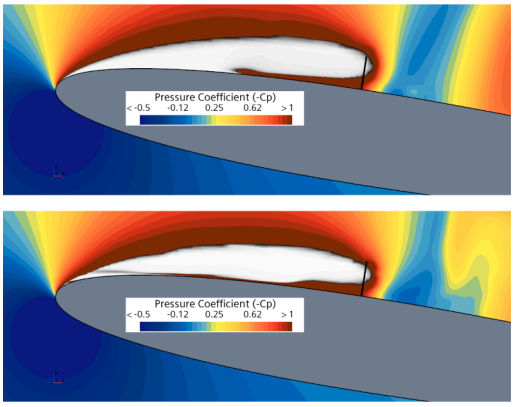

Fig. 7. Instantaneous pressure distribution near the cavity closure region. Top shows the model scale and bottom is full scale. Data is collected using a line probe (shown in black) positioned close the closure region.

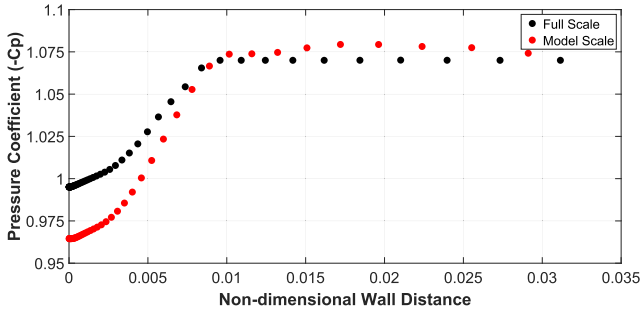

Fig. 8. Pressure distribution (-Cp) near the cavity closure for the instant shown in Fig. 7.

where $Y(x,t)$ is the matrix of the collected dataset, $a_i(t)$ are the temporal coefficients, and $\phi_i(x)$ are the spatial modes ordered in descending order of their energy content. In this context, $Y(x,t)$ represents the collected two-dimensional snapshots of the attached cavity and cloud.

The snapshot method as formulated by Sirovich (1987) is used to compute the functions and coefficients. This approach uses Singular Value Decomposition (SVD) and the decomposition is expressed as,

$$Y(x,t) = \phi_i(x)\Sigma V^T. \tag{15}$$

Here, Σ is a diagonal matrix with entries corresponding to the singular values of the energy content of the modes in decreasing order. V^T is the transpose of the matrix V, where the columns represent the temporal evolution of the corresponding spatial modes. The programming language MATLAB is used to perform the decomposition and the procedure is as follows,

- The data matrix is constructed from flattened grayscale images of the vapor structures. Here, each column entry represents a single snapshot, and each row corresponds to a pixel across all snapshots. The resolution of the images corresponds to 512 x 256 with more than 4000 images.
- The mean is subtracted from each column before computing the covariance matrix $C = \frac{1}{n}Y^T Y$, where n is the number of snapshots.
- Eigen decomposition is applied on matrix C to obtain the eigenvalues λ_i and eigenvectors V.
- The temporal coefficients in matrix $a_i(t)$ are computed as $a_i(t) = \Sigma V^T$, where Σ is a diagonal matrix of $\sqrt{\lambda_i}$.
- Finally, the spatial modes $\phi_i(x)$ are reconstructed using Eq. (15).

Fig. 9 presents the obtained first five spatial modes for both model and full scale conditions. The percentages represent the cumulative energy contribution relative to the total energy. In the first two modes,

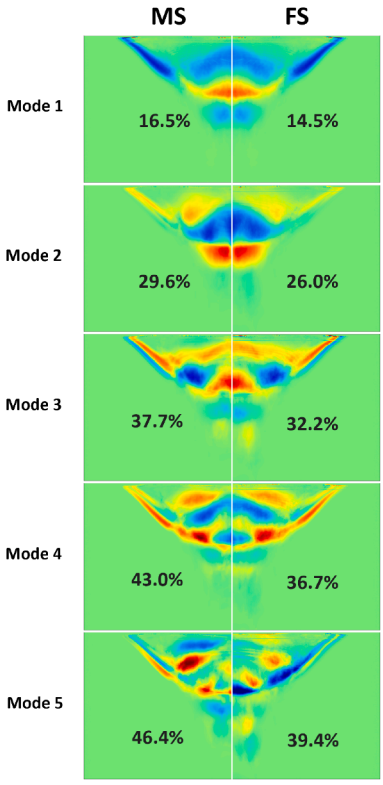

Fig. 9. Dominant POD spatial modes 1 through 5 (Percentages represent cumulative energy).

large-scale coherent spanwise rolling vortex and horse-shoe structures are dominant and contribute the highest energy. The region where the side-entrant jet interacts with the attached cavity is dynamic and present in all of the first five modes. For higher-order modes beyond the second one, coherent smaller-scale vapor structures are observed including vortices associated with the transported cloud. It is worth noting here that the relative cumulative energy distribution differs between the two scales. The lower percentages at full scale do not imply lower energy levels. Instead, it points to a broader energy distribution across the spectrum of the spatial modes due to the higher Reynolds number. Nevertheless, the first four modes are almost identical at both scales, which suggests that large-scale structures are not significantly influenced by scale effects.

Although large-scale structures are not influenced by scale effects, higher-order spatial modes presented in Fig. 10 indicate otherwise. Smaller-scale structures are now more pronounced but appear less coherent. While similarities appears between both scales at mode 7, other modes show more structures at full scale. For instance, in the last three modes, there are differences that appear near the leading edge and further downstream in the vicinity of the trailing edge, where more isolated structures are present. While this is associated with the Reynolds number, it indicates that on average the cloud is transported further downstream at full scale due to enhanced mixing effects from the small-scale structures. To summarize, scale effects are more pronounced in small-scale structures while the shedding mechanism and dominant structure remain similar.

4.1.4. *Power spectral density of induced pressure fluctuations*

The shedding of the attached cavity, its dynamics, and the collapse of the vapor structures will induce hydrodynamic pressure fluctuations. To evaluate the influence of scale effects on these fluctuations, three virtual pressure transducers were mounted on the top wall of the computational domain at the midspan of the foil. The transducers are located at 10 %, 50 %, and 100 % of the chord length. Pressure data was collected for 15

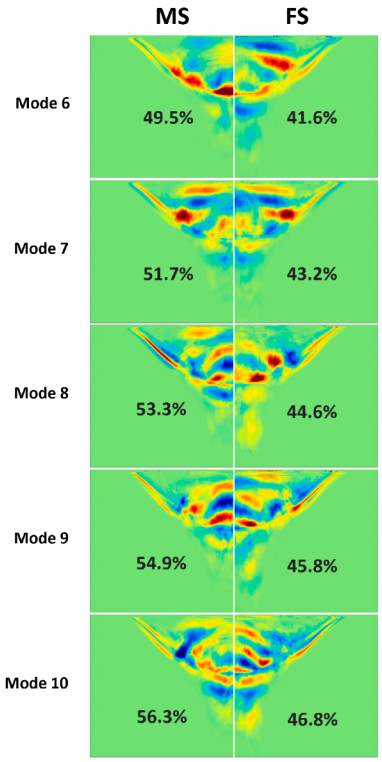

Fig. 10. Higher-order POD modes (6–10) (Percentages represent cumulative energy).

shedding cycles and normalized to obtain the pressure coefficient. The Fast Fourier Transform (FFT) is then applied to the pressure coefficient data to compute the Power Spectral Density (PSD) in decibels per Hertz (dB/Hz). In addition, the frequency is normalized by $f^* = \frac{fc}{U}$, where c and U are the foil chord length in meters and free stream velocity in meters per second.

Fig. 11 presents the computed PSD of the induced pressure fluctuations for both model and full scale conditions. Data from the virtual transducer positioned at the mid chord is only presented here as similar results are obtained with the others. Results indicate the influence of the scale effects on the energy content of the pressure fluctuations which is greater at the full scale condition across the entire frequency spectrum.

The first peak in the signal corresponds to the predicted shedding frequency with difference of approximately 15 dB/Hz. It is interesting to point out that the peak is also slightly shifted between both scale conditions. Other smaller peaks follow which are possibly associated with the collapse of the smaller scale cavitation structures. However, it is interesting to see that those higher frequency peaks are still very similar between both scales, say for instance at 1.5 and 2.9 of the non-dimensional frequency. This indicates that the global behavior of the shedding mechanism is not significantly changed by scale effects. However, the overall power is higher at full scale, suggesting a more energetic and intense cavitation collapse. At high frequencies, the PSD levels are higher for the full scale conditions due to the higher Reynolds number and more pronounced smaller-scale structures.

4.2. Cavitating propeller behind ship hull

4.2.1. Scale and blockage effects on wake field distribution upstream propeller

The operation of a propeller within the wakefield induces spatial and transient load variations on the propeller blades which affects the developed cavitation. Accurately simulating the wake distribution is then obviously essential for reliable predictions of propeller performance and

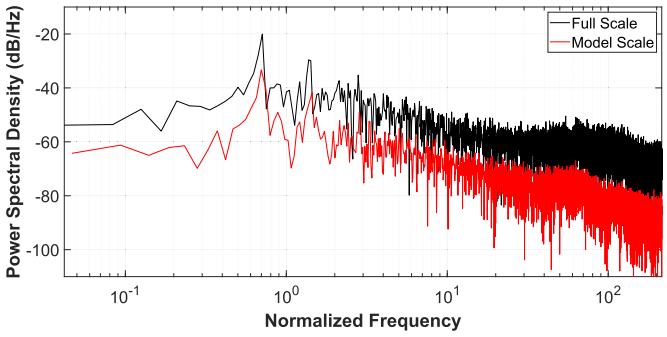

Fig. 11. Power spectral density of the induced hydrodynamic pressure fluctuations at model and full scale conditions.

cavitation dynamics. One of the main limitations of model scale tests is the impracticality of obtaining Reynolds number similarity with full scale conditions as mentioned earlier. As a consequence, the difference in the development in the boundary layer relative to full scale results in significant changes to the wakefield and loading conditions on the propeller. Understanding the scale effects on wakefield distribution is important as these effects are directly linked to the cavitation development and its characteristics. In addition to scale effects, model tests are typically performed in small or medium-sized cavitation tunnels. The restrictions from the tunnel walls will also directly influence the velocity and pressure distributions, a phenomenon known as blockage. The definition of blockage takes the ratio of the maximum cross-sectional area of the model ship and the cavitation tunnel section. As described previously, the model scale experiments are performed by RISE in their cavitation tunnel, and blockage for this case is 10.15 %. While this value remains well below the 20 % threshold recommended by ITTC guidelines for model scale testing, numerical results suggest that even at 10 %, blockage effects remain significant as discussed in the following section.

Fig. 12 presents the predicted axial velocity distribution, normalized by the free stream velocity, at a cross-sectional plane located at 0.48R upstream of the propeller plane for both model scale (Tunnel Section and Large Domain) and full scale conditions. A comparison of the velocity distribution at the wake peak region corresponding to the blade's 12 o'clock position shows the strong influence of scale effects. The wake peak region refers to the region of the lowest axial velocity magnitude, colored in blue in the contour plots. Here, the wake peak region is slimmer at full scale. This variation is attributed to the difference in the Reynolds number that influences the development and thickness of the boundary layer. At model scale, the lower Reynolds number leads to a thicker boundary layer which increases the displacement effect for the velocity field in this region. Another interesting observation away from the wake peak region that appears more pronounced at full scale is the asymmetry in velocity distribution between the angular positions of 90° and 270°. The flow appears to have a higher velocity magnitude at the 90° position. This asymmetry is due to the favorable flow direction coming from the hull's underbody and opposing the direction of the blade rotation. As a result, the apparent velocity over the blade suction side is higher, leading to a stronger pressure drop on the blade surface and generating higher suction force. At the model scale Tunnel Section (TS), the wakefield is affected by the domain size due to blockage effects. The velocity field distribution is changed significantly in all positions when compared with the Large Domain (LD). The space constraint from the side and bottom walls of the tunnel accelerates the flow into the propeller plane. This is particularly more pronounced in the region at the angular positions between 90° and 270° where the wakefield appears broader with the LD condition. While the LD condition provides a closer approximation of the full scale wakefield, scale effects remain significant enough to influence the velocity distribution.

Fig. 13 provides additional details on the predicted axial wake distribution across propeller radial positions from 0.3R to 1.0R, where R

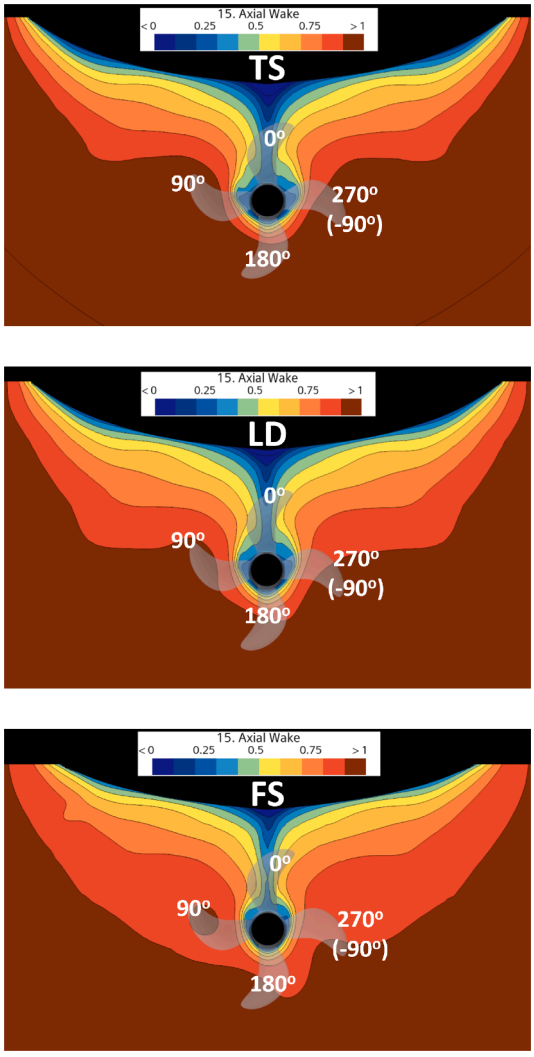

Fig. 12. Axial wakefield distribution on a cross-section positioned 0.48R upstream the propeller plane for Tunnel Section (TS), Large Domain (LD), and Full Scale (FS) conditions.

is the propeller radius. While the wake peak region shows similar velocity distributions between the TS and LD conditions, the TS condition has a slightly larger velocity deficit at the wake peak. This means that the blade will experience slightly higher loading in this region with TS conditions. The weak peak differs more significantly at full scale which features a smaller velocity deficit, indicating less loading on the propeller blade. Away from the wake peak, velocity recovery is slower at full scale. Here, velocity recovery refers to the rate at which axial velocity increases radially outward from the wake peak. As a result, the blade is expected to experience increased loading at these positions compared to the model scale. When comparing LD with TS, velocity recovery is slower with the former due to the diminished effect from the tunnel walls. These variations will directly influence the blade loading distribution as discussed in the subsequent section.

In addition to the axial wake component, the vertical component at various radial positions is presented in Fig. 14 on a plane 0.48R away from propeller disc. The influence of the vertical component on the propeller performance becomes more pronounced away from the peak region when it is nearly tangential to the blade surface, particularly when the blade is at the 90° and 270° positions. As mentioned previously, the flow direction at 90° relative to the blade rotation is favorable whereas it is unfavorable for the 270° position. Differences between the TS, LD and FS conditions are pronounced. Beyond 0.7R, the vertical velocity magnitude is lowest at the full scale condition relative to model scale. This scale effect may be associated with the weaker vortical structures (bilge vortices) entering the propeller plane at higher Reynolds number (Fu et al., 2011), which could influence the vertical velocity magnitude as observed.

4.3. On the influence of blockage on propeller performance

Fig. 15 presents the pressure distribution on the blade suction side (top) and back side (bottom) for both TS and LD conditions. The limiting streamlines shown in black represent the vector direction of the wall shear stress. In addition, the developed cavitation appears at the 0° position and is represented by a white transparent isosurface set at $\alpha_v = 0.5$. Results are shown for four angular positions: 0° , 90°, 180°, and 270°. Here, 0° corresponds to when the blade is at the 12 o'clock position and rotates clockwise from upstream.

On the suction side, the flow behavior over the blade surface remains broadly similar between the TS and LD conditions. Flow separation occurs near the trailing edge, and extends from the blade root to approximately 0.85R in both cases. At the 0° position, the presence of the sheet cavity influences the flow as the re-entrant jet is being driven underneath the cavity by the pressure gradient. More pronounced differences appear on the suction side pressure distribution. The blade in the TS condition has a lower pressure level across all different angular positions. This discrepancy in pressure level will influence cavitation inception, particularly where local pressure magnitude falls below vapor pressure. In addition, while the lower pressure magnitude might suggest higher loading in the TS condition, such a conclusion is premature without accounting for the back side, as shown in the lower part of Fig. 15.

The pressure distribution on the back side is also influenced by blockage. Across all angular positions, the pressure level is higher in the LD condition. Since the thrust magnitude generated by the blade depends on the pressure difference between the suction and back sides, the overall mean loading on the propeller remains similar between the two conditions with thrust similarity achieved as shown in Table 2. At the 0° position, the flow on the pressure side remains attached to the blade surface and is largely not affected by blockage. However, as the blade rotates away from the wake peak region toward the 90° position, a backside vortex develops starting at approximately 0.5R. This vortex structure is associated with separated flow at the leading edge. The vortex becomes more pronounced at the 180° and 270° positions and is stronger in the TS as indicated by greater pressure drop in that region.

To investigate the influence of the back side vortex, Fig. 16 presents the pressure coefficient distribution at the 270° blade position for radial locations from 0.3R to 0.95R. On the y-axis, the mean is subtracted from the pressure coefficient to account for the induced shift by blockage observed in Fig. 15. The x-axis shows the chord position, with 0 and 1 representing the leading and trailing edges, respectively. The pressure distribution on the blade is similar between TS and LD conditions. However, more significant differences appear close to the leading edge. At 0.3R, the blade at TS conditions is more heavily loaded, as indicated by the larger area under the curve from the leading edge to about 0.5 of the chord length. At radial positions of 0.5R and 0.7R, the influence of the pressure side vortex is more pronounced. At these radial positions and up to 0.05 of the chord length, a drop in pressure occurs on the blade back side which is lower than the levels on the suction side. The effect is more pronounced at 0.9R and 0.95R where the drop in pressure is larger and induces a reverse thrust in that specific region, affecting the blade performance. This adverse effect from the back side vortex is greater at TS condition. In addition, at 0.95R and between chord positions 0.1 and 0.3, the LD condition indicates an earlier pressure recovery on the back side which increases the generated thrust from the blade.

Fig. 17 presents the thrust coefficient for a single blade across two blade passages. Model (TS and LD) and full scale conditions are shown together to highlight the influence of blockage and scale effects on transient thrust generation by one propeller blade. Results show a significant

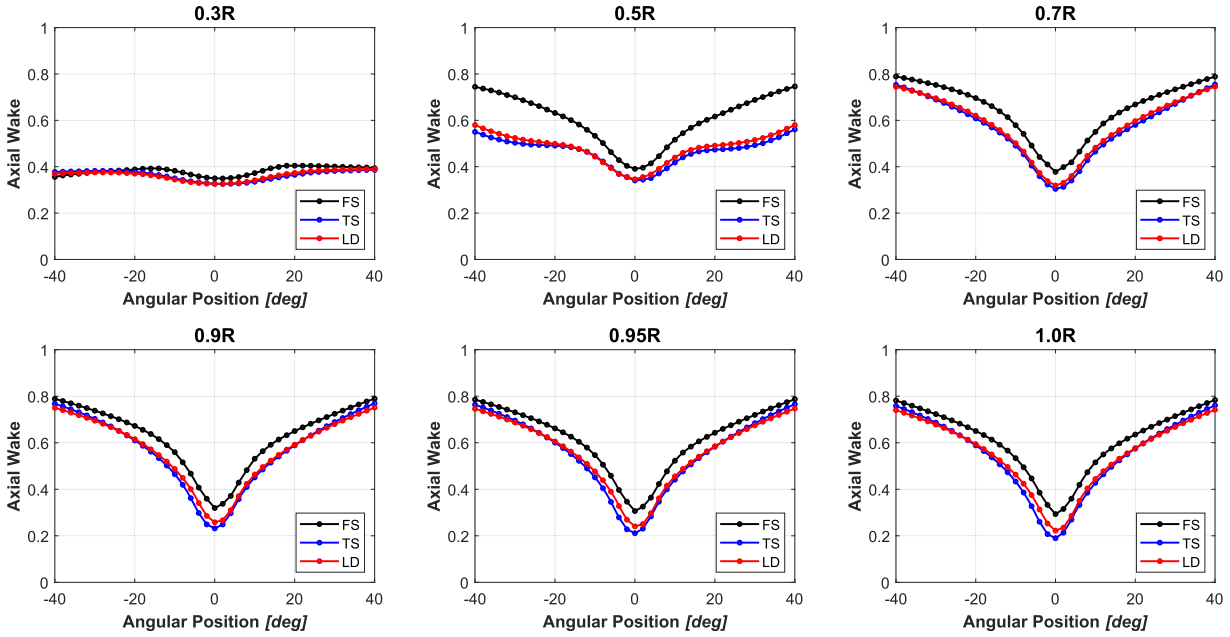

Fig. 13. Details of the axial wake distribution at different radial positions for Tunnel Section (TS), Large Domain (LD), and Full Scale (FS) conditions.

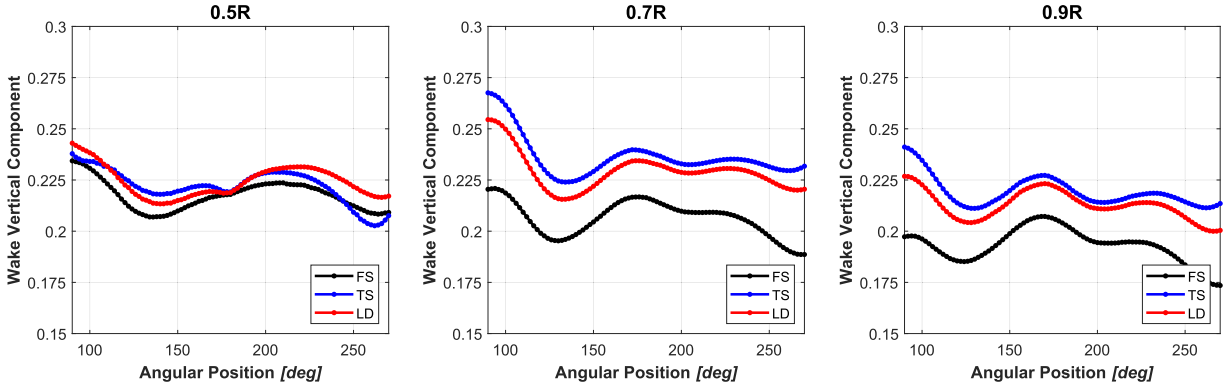

Fig. 14. Vertical component of wake distribution at different radial positions for Tunnel Section (TS), Large Domain (LD), and Full Scale (FS) conditions.

influence of both effects on thrust. Between angular positions of 0° and 90°, the blade is most heavily loaded in the TS condition, followed by LD and full scale conditions. This trend matches the wakefield distribution characteristics discussed earlier. Sheet and tip vortex cavitation develops within the wake peak region and up to 50°. As a result, the variations in the thrust and blade loading will influence the developed cavitation. After the blade exits the wake peak region, a shift in thrust magnitude is observed. The blade in the TS condition produces lower thrust compared with LD and full scale conditions between the 90° and 270° positions. This shift is associated with the variation in the spatial distribution of velocity due to the presence of the walls. In summary, while the mean loading on the propeller remains similar between the different conditions, the transient loading is affected by blockage and scale effects. These differences will influence cavitation inception, dynamics, and collapse, as discussed in Section 4.5.

4.4. Wetted flow pressure pulse levels

Before presenting scale effects on cavitation, it is useful to first consider scale effects on the pressure pulse levels for the wetted flow conditions. The pressure fluctuation time histories were collected for all eight transducers. To compare model and full scale results, pressure levels are non-dimensionalized using the scaling relation for the coefficient $K_{p(\phi)}$. This coefficient is assumed constant for each blade rate harmonic at both scales,

$$K_{p(\phi)} = \frac{P_\phi}{0.5\rho n^2 D^2}, \tag{16}$$

where P_ϕ is the pressure amplitude at the ϕ blade rate harmonic component obtained through the Fast Fourier Transformation (FFT) , ρ is the density, n is the rotation rate, and D is the propeller diameter.

Fig. 18 shows the predicted wetted flow 1st-order Blade Passing Frequency (BPF) pressure pulse levels for model scale (TS and LD) and full scale conditions together with experimental measurements. Small differences are observed among the CFD results. The full scale condition generally shows the lower levels, followed by the LD and TS conditions. The spatial distribution of pressure pulse levels is generally consistent with the measurements. The highest levels are at transducers G, D, and C. However, the deviation from experimental measurements varies by transducer location.

4.5. Predicted cavitation pattern on the propeller

The cavitation behavior during the model tests was observed to be unstable and intermittent for each blade passage. While dynamic wakefield and water quality contribute to this variability, the intermittency

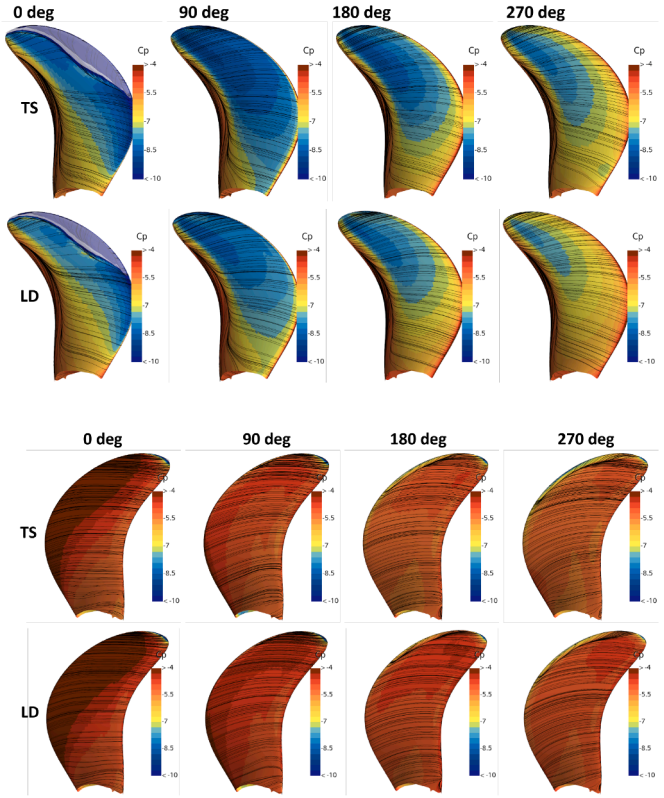

Fig. 15. Pressure distribution on the blade suction (top) and back (bottom) sides at model scale for Tunnel Section and Large Domain conditions. Limiting streamlines shown on black represent the vector direction of the wall shear stress and cavitation is visualized with isosurface $\alpha_v = 0.5$.

is primarily due to the low Reynolds number at which the blade operates. The laminar boundary layer suppresses cavitation inception, even when local pressure falls below the vapor pressure threshold. Due to this intermittency in model tests, comparing instantaneous snapshots with numerical predictions is not suitable. Instead, sketches are prepared as shown in Fig. 19 for comparison with numerical results. Cavitation patterns from the numerical results are generated using an isosurface defined by $\alpha_v = 0.5$. Figures are presented for blade positions starting at 0° (the 12 o'clock position) and rotating clockwise as viewed from upstream.

As the blade enters the wake peak region at the 0° position, an attached sheet cavity develops on the blade suction side. In the experiments, the sheet surface is smooth with isolated structures at varying inception points near the leading edge. Numerical prediction for the same condition predicted a continuous sheet structure that incepts at a lower radial position. For the CSR condition, the model and full scale cavitation patterns demonstrate the influence of scale and blockage effects on the developed cavitation. Cavitation extends the most and covers the largest area of the blade for TS condition, which is most heavily loaded at the wake peak. A smaller area is covered by the sheet cavity with the LD condition, followed by the full scale condition. Such variations are associated with discrepancies in the wake and pressure distribution, as previously discussed. As the blade rotates and reaches the 10° position, the sheet structure continues to grow in radial and tangential directions. In both experiments and numerical predictions, the sheet surface is smooth, but features an uneven surface with a convex shape at the closure region. A small tip vortex cavity starts to develop at this position for the CSR condition and appears more pronounced at the model scale relative to the full scale. By the 20° position, the sheet cavity begins to roll into a vortex structure in the experiments, with good agreement obtained from the numerical predictions. Both experiments and predictions also show a developing tip vortex cavity structure at this position. At CSR condition, the sheet has not collapsed yet, but similar comments on the extent scale and blockage effects on the extent of the sheet cavity can be made.

At the 30° position, the tip vortex cavity becomes more pronounced in all conditions. While the experiments show a continuous tip vortex structure, the numerical predictions show more broken up cavitation in the vortex. At the CSR TS condition, the sheet collapse is delayed due to its larger size, but the tip vortex is most dynamic with multiple bursting events. At full scale, the sheet collapses earlier, leaving a smaller and isolated tip vortex structure. By the 40° position, the sheet cavity has fully collapsed across all conditions and only tip vortex structures remain. In the experiments, the dynamic tip vortex is observed until the 60° position but has dissipated before 50° in the numerical predictions. The tip vortex is highly dynamic at the CSR condition with multiple events of growth and collapse. Although the CSR TS snapshot at this position shows no tip vortex vapor structure, multiple cycles of events occur later. At this specific position, the tip vortex structure appears more pronounced at the LD which reflects the influence of the change in the wakefield on the tip vortex dynamics. At full scale, the tip vortex appears thinner, less dynamic and collapses earlier than at model scale. While this is possibly related to the sharper wakefield, the spatial resolution also affects the numerical diffusivity of the tip vortex structure. Furthermore, the numerical models do not account for the laminar boundary layer on the blade surface at the model scale which influences the tip vortex strength.

4.6. Cavitation induced pressure fluctuations and pulse levels

Pressure fluctuation time history due to the cavitation dynamics and collapse are presented in Fig. 20 for model and full scale CSR conditions for two blade passages. The influence of blockage and scale effects are reflected in the characteristics of the induced pressure signal. The first peak in the pressure signal comes from the collapse of sheet cavitation, which occurs around the 27° position. The amplitude and timing of this collapse differ across the three conditions. The highest first peak amplitude is recorded from the TS with the collapse occurring at a slightly delayed time compared to the LD and full scale conditions. This delay and higher intensity are due to the larger sheet cavitation predicted. In contrast, the sheet cavitation collapse in the LD condition happens slightly earlier with a much lower intensity. At full scale, the blade experiences the lowest loading at this position, and the sheet collapse shows the lowest peak amplitude which occurs at a time closer to the LD condition.

After the sheet cavitation collapse, a series of pulsating events follow from the dynamic behavior and bursting of tip vortex cavitation. The intensity and timing of these tip vortex dynamics vary across the TS, LD, and full scale conditions. The tip vortex bursting shows the highest peak amplitude and a noticeable delay for the TS condition. The amplitude of the tip bursting event is nearly as intense as the sheet collapse. Interestingly, the tip vortex appears more affected by blockage than scale effects. However, it's worth noting again that the modeling approach assumes fully turbulent flow over the blade surfaces. Between the LD and full scale conditions, the amplitudes of the first and second tip vortex bursting events are similar, but their timing shifts slightly across blade passages. Although the tip vortex cavitation at full scale appears smaller than at the LD condition, their induced pressures are nearly equivalent in magnitude.

Numerical predictions for the harmonic components of the pressure pulse levels under cavitating conditions are presented in Fig. 21 together with experimental measurements. The results are presented for all eight transducers across all conditions. During the experiments, the pulsating levels showed little influence from cavitation and were similar to those obtained in the wetted flow conditions. In contrast, numerical simulations indicate an increase in pressure pulse levels of about 20 %, depending on the transducer location.

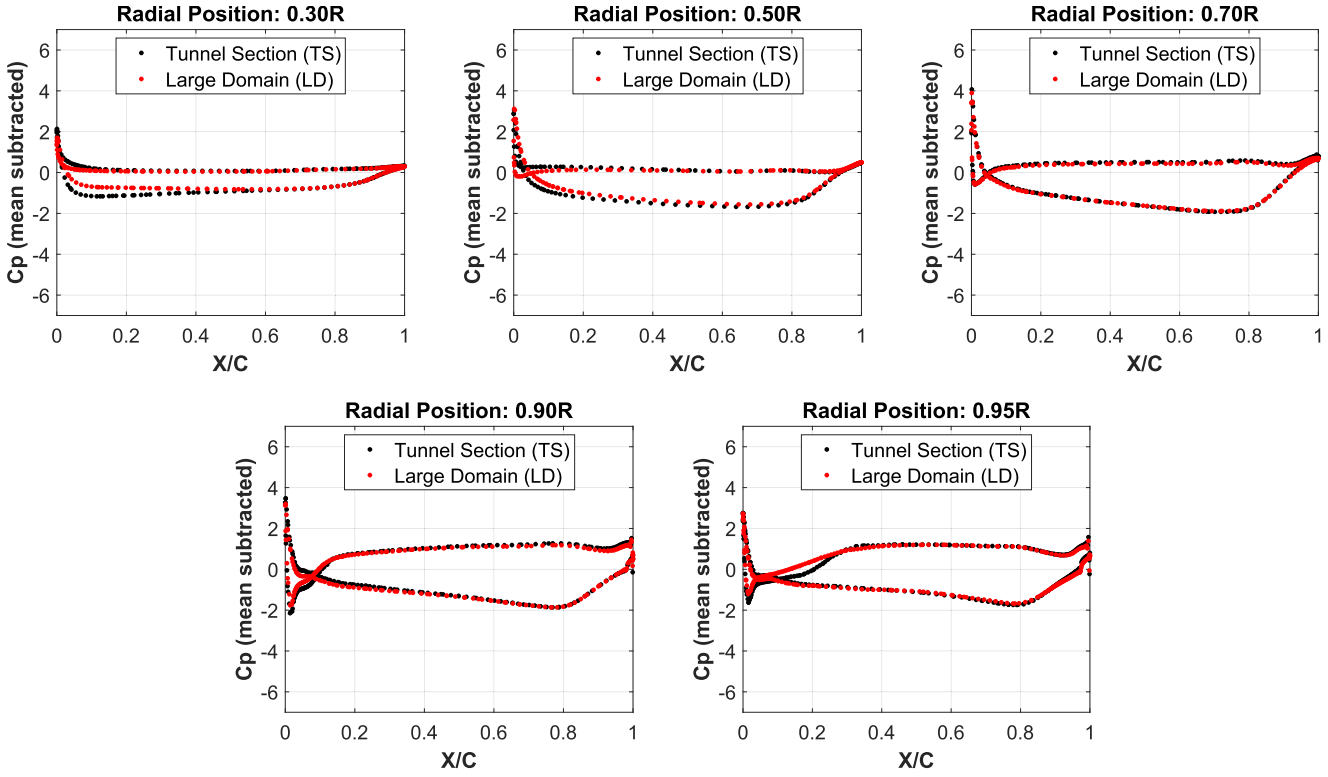

Fig. 16. Pressure distribution for various radial locations along the blade at the 270° position.

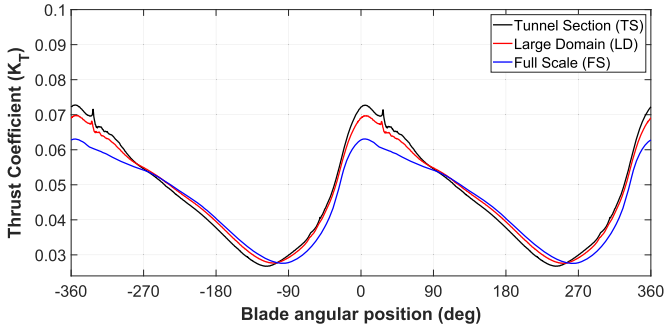

Fig. 17. Thrust coefficient history for a single blade at model scale (tunnel section and large domain) and full scale conditions.

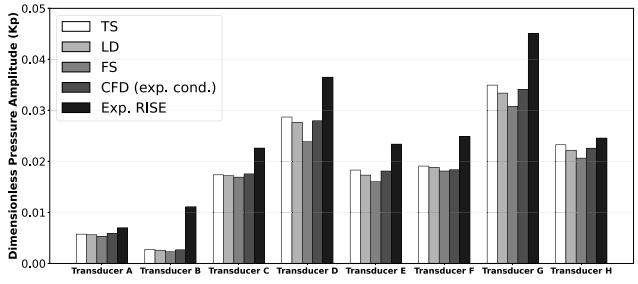

Fig. 18. First-order pressure pulse levels at wetted flow condition for all transducers.

Comparing the 1st-order pressure pulses, the numerical results underpredict the levels compared to the experiments, with relative differences varying by transducer placement. Even for the CSR condition where the propeller is slightly more loaded, lower levels are obtained relative to the experiments. This is associated with the stable wakefield predicted by the RANS approach, which affects the intensity of the cavitation collapse. Nevertheless, the spatial distribution of the recorded levels across the transducers aligns with the experimental data. As expected, the highest levels are recorded at the TS condition, followed by the LD and full scale conditions, which again reflect the influence of blockage and scale effects. For the LD, pressure pulse levels decreased by about 15 % at the two highest recorded transducers (G and D). The predicted pressure pulse levels at the full scale condition are lower than the model scale across all transducers. For instance, the predicted pulse level at the full scale is about 32 % lower than at the LD condition for transducer D. This trend is opposite to previous findings in the literature, which generally indicate that cavitation extent and the associated pressure pulse levels increase with scale. Note that our results for the hydrofoil are in line with observations in the literature. We believe the reason is that prior studies, as well as the foil here, were performed in open water configurations, while for the propeller in behind the scale effects on the wakefield and its interaction with the propeller dominate and thus yields reduced cavitation volume.

Higher-order pressure pulse levels are shown in Fig. 22 for transducer D for all conditions. While numerical simulations underpredict the 1st-order pressure pulse levels, they overpredict the higher-order components compared to experiments. The intermittent cavitation observed in the experiments, where the cavitation occasionally does not develop, particularly for the tip vortex, will reduce the overall levels. This leads to larger discrepancies between numerical predictions and experimental measurements for these higher-order components. For the CSR condition, blockage and scale effects remain significant, consistent with the trends observed for the 1st-order pressure pulse levels discussed earlier.

4.7. *On the influence of wall functions for full scale simulations*

Simulating high Reynolds number flows, such as those around full scale ships, is challenging due to the presence of thin boundary layers. Resolving the boundary layer requires maintaining y^+ values below 1.0 for the near-wall cell. This demands high spatial resolution in the wall-

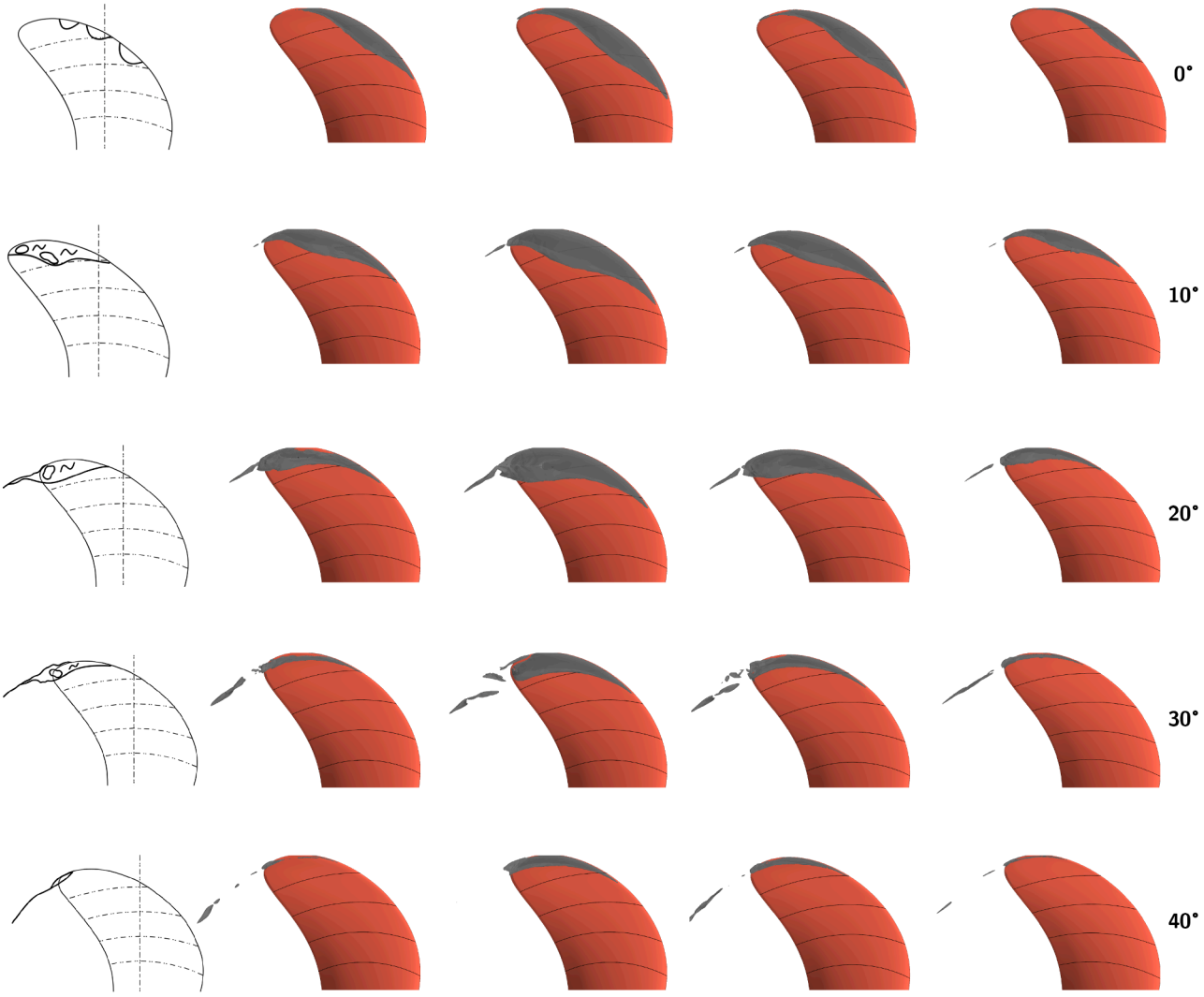

Fig. 19. Cavitation patterns arranged left to right: model scale experiments, CFD RISE Condition, CSR Tunnel Section (TS), CSR Large Domain (LD), and CSR Full Scale.

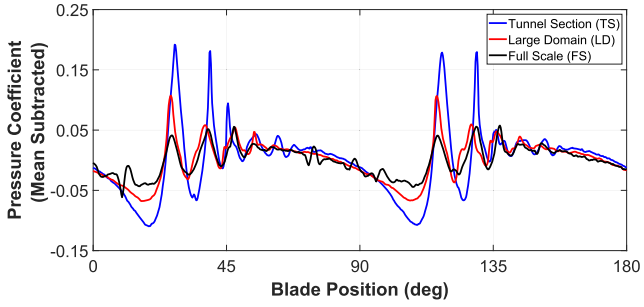

Fig. 20. Time history of induced pressure fluctuations at transducer D over two blade passages for model scale (Tunnel Section and Large Domain) and full scale conditions.

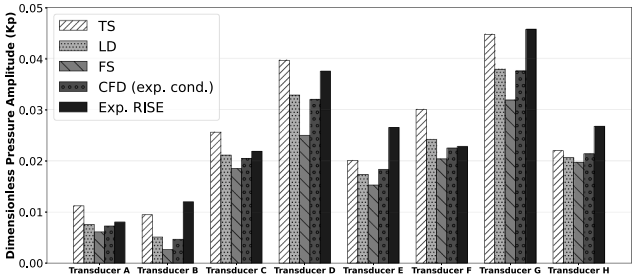

Fig. 21. First-order pressure pulse levels at cavitating flow condition for all transducers.

normal direction, leading to cells with high aspect ratios. Apart from potential numerical stability limitations, the increase in the total cell count requires high computational resources. An alternative approach to overcome these issues is the use of wall functions. Instead of resolving the boundary layer, wall functions apply semi-empirical formulas to estimate the near-wall flow field. However, this may compromise the accuracy of the computed flow field due to the assumptions involved. Wall functions assume a universal logarithmic velocity profile, making them unsuitable for flows with adverse pressure gradients (Wilcox, 2006). This is important as re-entrant jets forming underneath attached cavities are typically driven by adverse pressure gradients. There is also the risk that the re-entrant jet flow will not be sufficiently resolved, while further not be well characterized by the wall-function formula. In addition, wall functions are not suitable for separated flows and cases with strong curvature. While wall functions have been previously shown to achieve reliable predictions for propeller performance (Kim et al., 2021), this

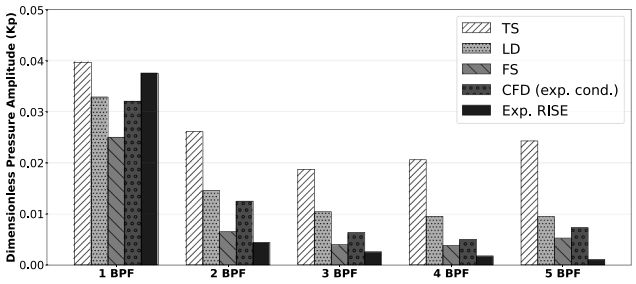

Fig. 22. Pressure pulse levels of the first five BPF components at transducer D.

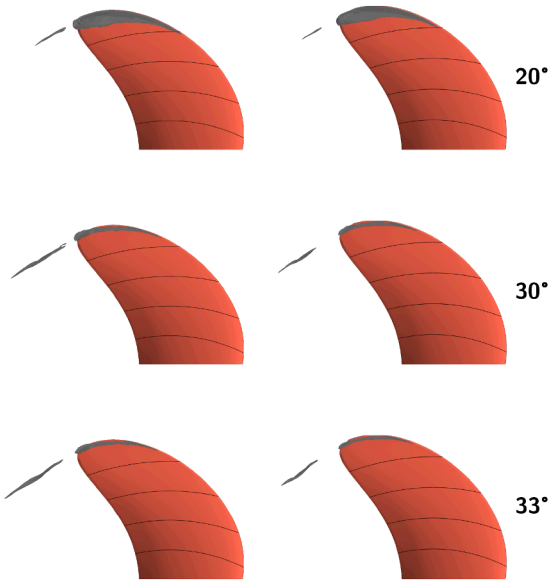

Fig. 23. Predicted cavitation patterns at full scale condition: Wall Resolved (left) and Wall Function (right).

study aims to assess their capability to predict the dynamics of sheet and tip vortex cavitation. The surface and tip vortex grid resolutions are kept constant, with only the wall-normal cell size adjusted to suit the wall function approach.

Fig. 23 shows instantaneous snapshots of the predicted cavitation patterns at the full scale condition using both the wall-resolved (WR) and wall-function (WF) approaches. Compared to WR, the WF approach underpredicts the vapor volume for both sheet and tip vortex cavitation. The difference is more pronounced for the tip vortex and its dynamics appear smaller and weaker. Given that the tip vortex spatial resolution remains similar in both approaches, the influence of wall treatment on the tip vortex characteristics is important to highlight. This is particularly important in the context of underwater radiated noise, where the tip vortex dynamics forms a significant noise source. As the WF approach underpredicts the size and strength of the cavitation, it is likely to underestimate underwater radiated noise levels.

To investigate the reason for the underprediction of the tip vortex with the WF approach, Fig. 24 shows pressure coefficient and non-dimensional vorticity at various cross-sections for when the blade is at the 15° position. Tip vortex flow structures are represented with an iso-surface of the *Q*-criterion set at 5000.

The isosurfaces of the vortex structures show clear differences based on the wall treatment. With the WR approach, three distinct tip vortex structures are predicted, two of which later merge into one. In contrast, the WF approach does not capture the bottom vortical structure. The non-dimensional vorticity planes further show that the vorticity magnitude with the vortex core is weaker with the WF. Comparing the maximum vorticity magnitude at each plane cut, the WF underpredicts vortex

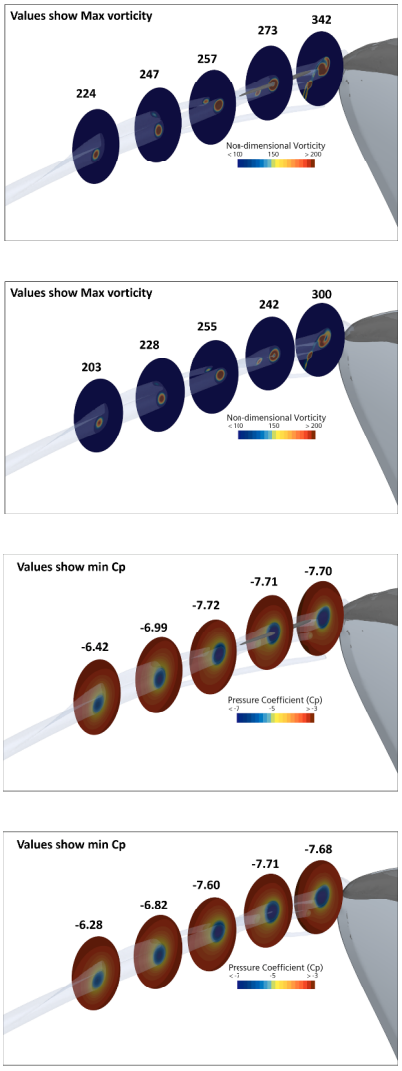

Fig. 24. Non-dimensional vorticity and Pressure coefficient at various cross-sections for when the blade is at the 15° position: Compariosn of the Wall Resolved (top) and Wall Function (bottom) approaches.

strength by 12 % in the first two cuts, where vapor structures develop. The minimum pressure within the vortex core is also consistently higher with the WF. As a result, a smaller and weaker tip vortex vapor structure with modified dynamics is predicted. Although the grid resolution for the tip vortex and blade surface remains similar, the wall-normal resolution is different. This suggests that the underprediction of the tip vortex may originate from unresolved interactions between the re-entrant jet flow over the blade surface and the tip vortex.

5. Conclusions

In this study, numerical simulations are performed to investigate scale effects on cavitating flows for two test cases. The first case is the Delft Twist 11 hydrofoil, which is characterized by unsteady shedding and cloud cavitation. To study scale effects, a geometrically scaled hydrofoil that is 20 times larger than the model scale is used. The corresponding Reynolds numbers for model and full scale are 1.1×10^6 and 2.58×10^7, respectively. Numerical results are compared with model scale measurements from TU Delft and EPFL cavitation tunnels. The average pressure distribution on the upper surface of the hydrofoil is over-predicted in the simulations compared to the experimental data, correlating to an underprediction of the cavitation extent. Analysis of scale

effects shows a longer cavity extent at full scale, which is associated with different pressure levels near the closure region compared with model scale. At full scale, the cavity detaches at an earlier time instant. This is attributed to the re-entrant jet having larger momentum, partly due to the reduced viscous losses at the higher Reynolds number condition. Further analysis using Proper Orthogonal Decomposition on cavitation shows that scale effects are more pronounced in smaller-scale structures, while the shedding mechanism and dominant structures remain similar.

The second test case focuses on scale and blockage effects on a cavitating propeller flow operating in a ship wake. Model scale tests were conducted by RISE in their cavitation tunnel and the results are used in a comparison with the numerical predictions. To assess blockage effects at model scale, two computational domains are used. The smaller domain is named Tunnel Section and is sized to match the dimensions of the test section during the experiments. The other is named Large Domain where the boundaries have been extended further away from the model ship. Although ITTC recommends blockage below 20 %, the numerical results show that blockage as low as 10 % still have significant effect on the flow. The wakefield distribution is sensitive to both scale and blockage effects, which influences the transient loading on the propeller blades, even when the mean loading is similar. The influence of scale effect on the wakefield distribution is mainly attributed to the differences in the boundary layer development, while the influence of blockage is associated with the constraints from the tunnel walls accelerating the flow into the propeller disc. Cavitation patterns reflect these effects as the sheet cavity extends furthest and covers the largest blade area with the TS, where loading is highest at the wake peak. A smaller area is covered at the LD condition, and even less at the full scale condition. This is an opposite trend compared with findings in the literature, where however previous studies were performed for an open water set-up and did not consider the influence of scales on the wakefield distribution and its interaction with the propeller. The tip vortex is also sensitive to both blockage and scale effects, appearing thinner at full scale. As a result, induced pressure fluctuations are lower at full scale compared to model scale conditions. Finally, a demonstration using wall function at full scale shows it underpredicts both sheet and tip vortex cavitation, making it unsuitable for such cases.

Our results indicate that there are effects on the cavitating flow on a propeller, working in behind conditions, from both model scale experiments and computations that are not considered in current scaling procedures. The origin is primarily changes in the wake field, due to scale effects as well as blockage in cavitation tunnel tests. Admittedly, there are no full scale data available to validate our findings, but we argue that the current computational techniques used are mature enough to give qualitatively robust results. However, there is a clear need for further studies, both computational and experimental, to quantitatively study these phenomenon.

CRediT authorship contribution statement

Qais Shehadeh Khraisat: Writing – review & editing, Writing – original draft, Visualization, Methodology, Investigation, Formal analysis; **Martin Persson:** Writing – review & editing, Supervision, Conceptualization; **Rickard E. Bensow:** Writing – review & editing, Supervision, Resources, Project administration, Methodology, Funding acquisition, Conceptualization.

Declaration of competing interest

The authors declare that they have no known competing financial interests or personal relationships that could have appeared to influence the work reported in this paper.

Acknowledgments

This project is funded by Kongsberg Maritime and the Swedish Transport Administration through Lighthouse Sustainable shipping program within the PUB project. The authors acknowledge Jan Hallander at RISE for the support with the experimental data from the tests he performed within the PUB project. The computations were enabled by resources provided by Chalmers e-Commons at Chalmers and by the National Academic Infrastructure for Supercomputing in Sweden (NAISS) at NSC partially funded by the Swedish Research Council through grant agreement no. 2022-06725.

References

Amromin, E., 2000. Analysis of viscous effects on cavitation. Appl. Mech. Rev. 53 (11), 307–322. https://doi.org/10.1115/1.3097332

Amromin, E.L., 2021. Modeling of the impact of laminar-turbulent transition on cavitation inception. Appl. Ocean Res. 114, 102796. https://doi.org/10.1016/j.apor.2021.102796

Apfel, R.E., 1970. The role of impurities in cavitation-threshold determination. J. Acoust. Soc. Am. 48 (5B), 1179–1186. https://doi.org/10.1121/1.1912258

Arabnejad, M.H., Amini, A., Farhat, M., Bensow, R.E., 2019. Numerical and experimental investigation of shedding mechanisms from leading-edge cavitation. Int. J. Multiphase Flow 119. https://doi.org/10.1016/j.ijmultiphaseflow.2019.06.010

Arakeri, V.H., Acosta, A., 1981. Viscous effects in the inception of cavitation. J. Fluids Eng. 103 (2), 280–287. https://doi.org/10.1115/1.3241733

Asnaghi, A., Bensow, R.E., 2020. Impact of leading edge roughness in cavitation simulations around a twisted foil. Fluids 5 (4). https://doi.org/10.3390/fluids5040243

Bensow, R.E., 2011. Simulation of the unsteady cavitation on the delft twist11 foil using RANS, DES and LES. In: Second International Symposium on Marine Propulsors.

Billet, M.L., Holl, J.W., 1981. Scale effects on various types of limited cavitation. J. Fluids Eng. 103 (3), 405–414. https://doi.org/10.1115/1.3240800

Coutier-Delgosha, O., Fortes-Patella, R., Reboud, J.L., 2003. Evaluation of the turbulence model influence on the numerical simulations of unsteady cavitation. J. Fluids Eng. 125 (1), 38–45. https://doi.org/10.1115/1.1524584

Duttweiler, M.E., Brennen, C.E., 2002. Surge instability on a cavitating propeller. J. Fluid Mech. 458, 133–152. https://doi.org/10.1017/S0022112002007784

Farkas, A., Degiuli, N., Martić, I., Dejhalla, R., 2019. Numerical and experimental assessment of nominal wake for a bulk carrier. J. Mar. Sci. Technol. 24, 1092–1104. https://doi.org/10.1007/s00773-018-0609-4

Foeth, E., 2008. The Structure of Three-Dimensional Sheet Cavitation phd thesis. Delft University of Technology, The Netherlands .

Foeth, E.-J., van Terwisga, T., 2006. The structure of unsteady cavitation part i: observations of an attached cavity on a three-dimensional hydrofoil. part II: applying time-resolved PIV to attached cavitation.(see attached files). In: Delft University of Technology, Ship Hydromechanics Laboratory, Faculty 3mE, Department of Marine Technology, Report No. 1537-PI, Paper of the 6th International Symposium on Cavitation, CAV'06, Wageningen, The Netherlands, September 2006.

Franc, J.P., Michel, J.M., 1985. Attached cavitation and the boundary layer:experimental investiguation and numerical treatment. J. Fluid Mech. 154, 63–90. https://doi.org/10.1017/S0022112085001422

Fu, T.C., Takinaci, A.C., Bobo, M.J., de Experiencias Hidrodinámicas, C., Gorski, W., Johannsen, C., Heinke, H.-J., Potsdam, S.-V., Kawakita, C., Wang, J.-B., 2011. The specialist committee on scaling of wake field. In: 26th International Towing Tank Conference.

Ge, M., Svennberg, U., Bensow, R.E., 2021. Improved prediction of sheet cavitation inception using bridged transition sensitive turbulence model and cavitation model. J. Mar. Sci. Eng. 9 (12). https://doi.org/10.3390/jmse9121343

Gindroz, B., Billet, M.L., 1998. Influence of the nuclei on the cavitation inception for different types of cavitation on ship propellers. J. Fluids Eng. 120 (1), 171–178. https://doi.org/10.1115/1.2819643

Gowing, S., Shen, Y.T., 2001. Nuclei effects on tip vortex cavitation scaling. In: Proceedings of the Fourth International Symposium on Cavitation (CAV 2001).

Hilo, A.K., Go, Y.-J., Hong, J.-W., Ahn, B.-K., Park, C., Kim, G.-D., Moon, I.-S., 2024. Cavitating flow control and noise suppression using air injection. Phys. Fluids 36 (8). https://doi.org/10.1063/5.0217652

Holl, J.W., 1970. Nuclei and cavitation. J. Basic Eng. 92 (4), 681–688. https://doi.org/10.1115/1.3425105

Huuva, T., 2008. Large Eddy Simulation of Cavitating and Non-Cavitating Flow. Ph.D. thesis. Chalmers University of Technology.

ITTC 7.5-04-04-01, 2024. Underwater noise from ships: Full scale measurements. https://www.ittc.info/media/11982/75-04-04-01.pdf.

Ji, B., Luo, X.-w., Wu, Y.-l., Liu, S.-h., Xu, H.-y., Oshima, A., 2010. Numerical investigation of unsteady cavitating turbulent flow around a full scale marine propeller. J. Hydrodyn. Ser. B 22 (5, Supplement 1), 747–752. https://doi.org/10.1016/S1001-6058(10)60025-X

Kamiirisa, H., 2001. The effect of water quality characteristics on cavitation noise. In: Fourth International Symposium on Cavitation, California Institute of Technology, Pasadena, CA USA.

Keller, A.P., 2001. Cavitation scale effects-empirically found relations and the correlation of cavitation number and hydrodynamic coefficients. http://resolver.caltech.edu/cav2001:lecture.001 .

Kim, K.-W., Paik, K.-J., Lee, J.-H., Song, S.-S., Atlar, M., Demirel, Y.K., 2021. A study on the efficient numerical analysis for the prediction of full-scale propeller performance using CFD. Ocean Eng. 240, 109931. https://doi.org/10.1016/j.oceaneng.2021.109931

Klapwijk, M., Lloyd, T., Vaz, G., van Terwisga, T., 2021. On the use of synthetic inflow turbulence for scale-resolving simulations of wetted and cavitating flows. Ocean Eng. 228, 108860. https://doi.org/10.1016/j.oceaneng.2021.108860

Korkut, E., Atlar, M., 2002. On the importance of the effect of turbulence in cavitation inception tests of marine propellers. Proc. R. Soc. London. Ser. A Math. Phys. Eng. Sci. 458 (2017), 29–48. https://doi.org/10.1098/rspa.2001.0852

Kuiper, G., 1978. Cavitation scale effects: a case study. Int. Shipbuild. Prog. 25 (284), 81–90. https://doi.org/10.3233/ISP-1978-2528401

Larsson, L., Raven, H.C., 2010. Ship resistance and flow. The Principles of Naval Architecture Series, Society of Naval Architects and Marine Engineers.

Li, D.-Q., Hallander, J., Johansson, T., 2018. Predicting underwater radiated noise of a full scale ship with model testing and numerical methods. Ocean Eng. 161, 121–135. https://doi.org/10.1016/j.oceaneng.2018.03.027

Menter, F.R., Kuntz, M., Langtry, R., et al., 2003. Ten years of industrial experience with the SST turbulence model. Turb. Heat Mass Transf. 4 (1), 625–632.

Moin, P., 1992. On the complexity of turbulence near a wall. In: Studies in Turbulence. Springer, pp. 223–228.

Ponkratov, D., 2015. Des prediction of cavitation erosion and its validation for a ship scale propeller. In: Journal of Physics: Conference Series. Vol. 656. IOP Publishing, p. 012055. https://doi.org/10.1088/1742-6596/656/1/012055

Reboud, J.-L., Stutz, B., Coutier, O., 1998. Two phase flow structure of cavitation: experiment and modeling of unsteady effects. In: 3rd International Symposium on Cavitation CAV1998, Grenoble, France. Vol. 26, pp. 1–8.

Regener, P.B., Mirsadraee, Y., Andersen, P., 2018. Nominal vs. effective wake fields and their influence on propeller cavitation performance. J. Mar. Sci. Eng. 6 (2), 34. https://doi.org/10.3390/jmse6020034

Sabnis, K., Babinsky, H., Spalart, P.R., Galbraith, D.S., Benek, J.A., 2021. Analysis and extension of the quadratic constitutive relation for RANS methods. Aeronaut. J. 125 (1292), 1746–1767. https://doi.org/10.1017/aer.2021.42

Sakamoto, N., Kamiirisa, H., 2018. Prediction of near field propeller cavitation noise by viscous CFD with semi-empirical approach and its validation in model and full scale. Ocean Eng. 168, 41–59. https://doi.org/10.1016/j.oceaneng.2018.08.061

Schnerr, G.H., Sauer, J., 2001. Physical and numerical modeling of unsteady cavitation dynamics. In: Fourth International Conference on Multiphase Flow. Vol. 1. ICMF New Orleans New Orleans, LO, USA, pp. 1–12.

Sezen, S., Atlar, M., 2022. Marine propeller underwater radiated noise prediction with the FWH acoustic analogy part 3: assessment of full-scale propeller hydroacoustic performance versus sea trial data. Ocean Eng. 266, 112712. https://doi.org/10.1016/j.oceaneng.2022.112712

Sirovich, L., 1987. Turbulence and the dynamics of coherent structures. i. coherent structures. Q. Appl. Math. 45 (3), 561–571.

Software, S. D.I., 2023. Simcenter STAR-CCM+ User Guide v. 2310. Siemens Digital Industries Software.

Soydan, A., Bal, S., 2021. An investigation of scale effects on marine propeller under cavitating and non-cavitating conditions. Ship Technology. Res. 68 (3), 166–178. https://doi.org/10.1080/09377255.2021.1883800

Spalart, P.R., 2000. Strategies for turbulence modelling and simulations. Int. J. Heat Fluid Flow 21 (3), 252–263. https://doi.org/10.1016/S0142-727X(00)00007-2

Su, X., Yuan, X., 2017. Improved compressor corner separation prediction using the quadratic constitutive relation. Proc. Inst. Mech. Eng. Part A J. Power Energy 231 (7), 618–630. https://doi.org/10.1177/0957650917709367

Szantyr, J., 2006. Scale effects in cavitation experiments with marine propeller models. Polish Maritime Res. 13, 3–10.

Tani, G., Aktas, B., Viviani, M., Atlar, M., 2017. Two medium size cavitation tunnel hydroacoustic benchmark experiment comparisons as part of a round robin test campaign. Ocean Eng. 138, 179–207. https://doi.org/10.1016/j.oceaneng.2017.04.010

Tani, G., Viviani, M., Felli, M., Lafeber, F.H., Lloyd, T., Aktas, B., Atlar, M., Turkmen, S., Seol, H., Hallander, J., Sakamoto, N., 2020. Noise measurements of a cavitating propeller in different facilities: results of the round robin test programme. Ocean Eng. 213, 107599. https://doi.org/10.1016/j.oceaneng.2020.107599

van Terwisga, T. J.C., van Rijsbergen, M., van Wijngaarden, E., Bosschers, J., Schenke, S., Melissaris, T., 2021. Cavitation nuisance in ship propulsion: a review of developments. Cavitation and Bubble Dynamics , 73–109. https://doi.org/10.1016/B978-0-12-823388-7.00011-4

Venning, J., Giosio, D., Smith, S., Pearce, B., Brandner, P., 2018. The influence of nucleation on the spectral content of cloud cavitation about a hydrofoil. In: 10th Symposium on Cavitation (CAV2018), pp. 1015–1030.

Venning, J., Smith, S., Brandner, P.A., Giosio, D., Pearce, B.W., 2017. The influence of nuclei content on cloud cavitation about a hydrofoil. In: International Symposium on Transport Phenomena and Dynamics of Rotating Machinery (ISROMAC 2017).

Viitanen, V., Siikonen, T., Sánchez-Caja, A., 2020. Cavitation on model-and full-scale marine propellers: steady and transient viscous flow simulations at different reynolds numbers. J. Mar. Sci. Eng. 8 (2), 141. https://doi.org/10.3390/jmse8020141

Wang, G., Senocak, I., Shyy, W., Ikohagi, T., Cao, S., 2001. Dynamics of attached turbulent cavitating flows. Prog. Aerosp. Sci. 37 (6), 551–581. https://doi.org/10.1016/S0376-0421(01)00014-8

Wilcox, D.C., 2006. Turbulence Modeling for CFD. DCW Industries, La Cañada, CA. 3rd ed.

Yang, Q., Wang, Y., Zhang, Z., 2013. Scale effects on propeller cavitating hydrodynamic and hydroacoustic performances with non-uniform inflow. Chin. J. Mech. Eng. 26 (2), 414–426. https://doi.org/10.3901/CJME.2013.02.414

Zhang, L., Chen, L., Shao, X., 2016. The migration and growth of nuclei in an ideal vortex flow. Phys. Fluids 28 (12). https://doi.org/10.1063/1.4972275